

Co-evolution of tumor cells and hepatocytes fostered by SLIT2-ROBO1 axis facilitates liver metastasis of pancreatic ductal adenocarcinoma

Qing Li

Shanghai Cancer Institute, Renji Hospital, Shanghai Jiao Tong University School of Medicine

Xiao-Xin Zhang

State Key Laboratory of Oncogenes and Related Genes, Shanghai Cancer Institute, Ren Ji Hospital, School of Medicine, Shanghai Jiao Tong University.

Li-Peng Hu

State Key Laboratory of Oncogenes and Related Genes, Shanghai Cancer Institute, Ren Ji Hospital, School of Medicine, Shanghai Jiao Tong University.

Bo Ni

Department of Gastrointestinal Surgery, Ren Ji Hospital, School of Medicine, Shanghai Jiao Tong University

Xu Wang

Affiliated Hospital, Jiangsu University

ShuHeng Jiang

Shanghai Cancer Institute, Renji Hospital, Shanghai Jiao Tong University School of Medicine

Min-Wei Yang

Department of Biliary-Pancreatic Surgery, Ren Ji Hospital, School of Medicine, Shanghai Jiao Tong University

Yong-shen Jiang

Department of Biliary-Pancreatic Surgery, Ren Ji Hospital, School of Medicine, Shanghai Jiao Tong University

Chun-Jie Xu

Department of Biliary-Pancreatic Surgery, Ren Ji Hospital, School of Medicine, Shanghai Jiao Tong University

Xueli Zhang

Ren Ji Hospital, School of Medicine, Shanghai Jiao Tong University <https://orcid.org/0000-0001-8306-0639>

Yanli Zhang

Ren Ji Hospital, School of Medicine, Shanghai Jiao Tong University <https://orcid.org/0000-0002-8942-5325>

Pei-Qi Huang

State Key Laboratory of Oncogenes and Related Genes, Shanghai Cancer Institute, Ren Ji Hospital, School of Medicine, Shanghai Jiao Tong University.

Qin Yang

State Key Laboratory of Oncogenes and Related Genes, Shanghai Cancer Institute, Ren Ji Hospital, School of Medicine, Shanghai Jiao Tong University.

Yang Zhou

Department of Obstetrics and Gynecology, Shanghai Jiao Tong University Affiliated Sixth People's Hospital

Jian-ren Gu

State Key Laboratory of Oncogenes and Related Genes, Shanghai Cancer Institute, Shanghai Jiao Tong University School of Medicine, Shanghai, Peoples Republic of China

Gary Gui-Shan Xiao

Functional Genomics and Proteomics Laboratory, Osteoporosis Research Center, Creighton University Medical Center

Yong-Wei Sun

Department of Biliary-Pancreatic Surgery, Ren Ji Hospital, School of Medicine, Shanghai Jiao Tong University, Shanghai, P.R. China <https://orcid.org/0000-0002-5937-634X>

Jun Li

<https://orcid.org/0000-0003-0423-3381>

Zhi-Gang Zhang (✉ zzhang@shsci.org)

Shanghai Cancer Institute, Ren Ji Hospital, School of Medicine, Shanghai Jiao Tong University

<https://orcid.org/0000-0001-8965-223X>

Article

Keywords:

Posted Date: December 21st, 2021

DOI: <https://doi.org/10.21203/rs.3.rs-76006/v1>

License:  This work is licensed under a Creative Commons Attribution 4.0 International License.

[Read Full License](#)

Version of Record: A version of this preprint was published at Nature Communications on February 15th, 2023. See the published version at <https://doi.org/10.1038/s41467-023-36521-0>.

Abstract

To explore the mechanism of co-evolution and potential driver of which in pancreatic ductal adenocarcinoma (PDAC) metastasis to liver, we studied key molecules involved in this progress and their translational values. Pre-metastatic niche (PMN) and macro metastatic niche (MMN) formation in mouse model were recognized via CT combined 3D organ reconstruction bioluminescence imaging. We next confirmed the expressions and distributions of SLIT2 and ROBO1 in 35 cases of human matched liver metastasis and primary PDAC samples, 14 case human PDAC liver metastasis transcriptional analysis, intrasplenic mouse models and *Kras*^{G12D}/*Trp53*^{R172H}/*Pdx1-Cre* (KPC) mouse models. Translational value was assessed on *Slit2*^{fl/fl}/*Alb1-Cre* (*Slit2* CKO) mice, KPC mouse model and *Ex vivo* tests via administration of neutralizing antibody targeting ROBO1. We also analyzed prognosis of 266 cases human PDAC tissue with or without SLIT2-ROBO1 fostered co-evolution and demonstrated the dependence receptor (DR) characteristics of ROBO1 in the following-up mechanism study. Experiments on *Slit2* CKO, *Slit2* CKO-RE and KPC mouse models demonstrated that disturbing SLIT2-ROBO1 mediated co-evolution in liver microenvironment via preventing their interaction could significantly attenuate liver metastasis of PDAC. We have demonstrated that co-evolution took advantage of DR characteristics in PMN and MMN. Targeting SLIT2-ROBO1 axis could be a therapeutic strategy towards metastatic PDAC.

Introduction

Patients diagnosed with PDAC bearing surgically resectable tumor account for less than 20% mainly due to its devastating metastatic nature, and liver is the most preferred destination of distant metastasis. Distant metastasis to specific target organ requires co-evolution between disseminated tumor cells (DTCs) derived from primary tumor and target organ microenvironment resident cells¹⁻². It has been illustrated by the hypothesis of “seed and soil” theory that the “seed” (DTCs) and “soil” (microenvironment of target organ) both adapted to each other for gaining the advantage to achieve metastasis³. According to this theory, co-evolution may take place between DTCs and hepatocytes in every step of PDAC liver metastasis to facilitate metastatic niche formation and expansion, while the driving power throughout this progress remain to discover. To uncover underlying mechanism, key events of continuous co-evolution involved in liver metastasis including PMN and MMN were selected for further study (Figure 1a)⁴⁻⁵. Recent studies have defined that PMN underwent complex tumor microenvironment (TMN) to adapt to “seeds” for their successful colonization, and formation of which was recognized as the initial step of metastasis progress. For metastasis, native cells at target organ altered original secretion protein profiles and began to recruit TMN cells to generate breeding ground before extravasation and implantation of tumor cells at PMN stage, though few morphological changes could be observed at these sites. Thus, it is hard to gain clinical samples of PMN formed liver of patients, and the means of PMN detection and definition were also limited. Here we utilized intrasplenic injection mouse model with relatively permanent PMN and MMN time points of PDAC liver metastasis and further verified our discoveries in KPC mouse model and clinical samples.

Members of Axon Guidance (AG) family have been considered to play vital roles in a variety of physiological processes such as embryonic development and neuron growth⁶⁻⁷. While accumulating evidence also revealed their indispensable functions in cancers⁸⁻⁹. Intriguingly, several important receptors of AG were reported to share common characteristics in different cancers, termed as DRs¹⁰⁻¹². DRs are kinds of special receptors acting as a two-way switch to trigger cell proliferation and survival in presence of their ligands, or induce apoptosis once ligands are moved off, rather than simply performing on and off. In normal conditions, it is generally supposed that DRs are responsible to maintain tissue homeostasis and prevent escape of cells from where they were^{11, 13}. Therefore, it is interesting to explore the mechanisms involved in DRs mediated metastasis. Though discussed in many previous studies, the meaning of existence of DRs in tumorigenesis, especially in metastasis remain largely unknown.

Here we filtered out AG molecular SLIT2 in our models which were overexpressed by hepatocytes through PMN to MMN and demonstrated for the first time that its classic receptor ROBO1 was a DR. We have also unveiled that hepatocytes derived SLIT2 formed a breeding ground for implantation of ROBO1 positive DTCs thus triggered co-evolution between hepatocytes and tumor cells for further MMN achievement. Interference of the interaction of these two molecules via neutralizing antibody could significantly hamper the progress of liver metastasis. Our results revealed a previously unknown role of DRs in metastasis of cancer and put forward that SLIT2-ROBO1 axis mediated co-evolution of “seed” and “soil” was critical in implantation and outgrowth on PMN till MMN. We also provided a potential therapeutic strategy to inhibit co-evolution via targeting DRs to not only prevent proliferation of tumor cells but also trigger their apoptosis.

Results

Detection and verification of PMN and MMN in mouse models

To set off, we utilized the intrasplenic injection mouse model to study alteration of liver microenvironment from PMN to MMN. In this model, injected tumor cells could generate liver metastatic lesions via passing through the portal veins to simulate PDAC liver metastasis which is highly reproducible and make it possible for us to analyze the step-by-step changes of expression profiles in liver¹⁴⁻¹⁵.

KPC mice derived PDAC cells Kpc1199 or murine PDAC cells Panc02 were performed to generate liver metastasis. Thus, we could cite the approximate time of metastasis process of Kpc1199 (D7-D11 for PMN and D12- for MMN) or Panc02 (D5-D8 for PMN and D9- for MMN) in intrasplenic injection model (Figure 1b, Extended Data Figure 1a; detailed methods on determination of PMN and MMN time points are shown in *Materials and Methods*). CT combined 3D organ reconstruction bioluminescence imaging provided the possibility of observation and precise location of tiny signal points of metastatic niches (Figure 1c-1e; Extended Data Figure 1a-1b). At time point of D8 for Kpc1199 or D6 for Panc02, PMN formed with few GFP⁺ cells, while the reported markers LOX, SAA1/2, TIMP-1, and MIF or CD68, CD11b

and CD163 for macrophages and Ly-6G for neutrophils expressions were observed, which was defined as PMN group. D15 for Kpc1199 or D12 for Panc02 witnessed IHC-detectable metastatic clones planting on liver which was recognized as metastasis group (Figure 1f-1h, Figure 2f; Extended Data Figure 1c-1k, Figure 3a) ¹⁶⁻²². Additionally, we selected D3 instead of D0 as control group to eliminate the interference of non-tumor inflammation of surgery among groups. The time point and location of metastases formed by PDAC cells on left hepatic lobule were relative reproducible due to the hemodynamic character of portal veins. In summary, we could thus gain liver tissues undergoing PMN and MMN in mouse models for further exploration.

Enriched hepatocytes derived SLIT2 is located with ROBO1 positive tumor cells in liver metastasis progress

Hence, to comprehensively investigate the differentially expressed genes of hepatocytes during process of PDAC metastasis, we set out to slice 2×2×2 mm³ of the liver tissue without tumor and close to portal veins in left hepatic lobule of mice at D3, D8 or D15 for Kpc1199 or D3, D6 or D12 for Panc02 after intrasplenic injection respectively. These specimens were further confirmed by positive staining of PMN markers before they were used for further studies (Figure 2a-2b). Then we performed transcriptomic analysis for these three groups. Gene Set Enrichment Analysis (GSEA) of transcriptome data on NL vs PMN or NL vs MMN highlighted the importance of axon guidance pathway in liver metastasis (Figure 2c). Further decipherment of secreted proteins of axon guidance family revealed common genes both upregulated in PMN and MMN-detected livers (*Sema3e*, *Slit2* and *Efna4*) (Extended Data Figure 2a-2c). Among these axon guidance secreted ligands, SLIT2 were filtered out in both PMN and MMN of two cell lines derived mouse models (Figure 2d; Extended Data Figure 2a-2c). Further results have shown that SLIT2 expression began to arise from PMN formation (D3~D7) and lasted until the completed metastatic colonization (D10~D15) in the adjacent area of metastatic niche (Figure 2e-2f). And same phenomenon could also be observed in Panc02 derived liver metastasis model (Extended Data Figure 3a). To further confirm, we used KPC mice, which could spontaneously generate liver metastasis of PDAC. We first detected DTCs in left hepatic lobule by measuring the PDAC DTCs markers CK19, CD133 and CD44 from KPC mice before 12 weeks old at which metastasis took place in frequency²³⁻²⁴ (Extended Data Figure 3b). The PMN markers mentioned above in intrasplenic injection model were also detected in the livers of KPC mouse with DTCs (Extended Data Figure 3c). Furthermore, highly expressed SLIT2 was also found in DTCs-detected PMN or MMN formed liver of KPC mice (Figure 2g-2h). To further confirm the source of SLIT2, staining of which on liver metastasis pathological slice of PDAC patients was performed. Adjacent liver of PDAC patients' metastatic niches exhibited enhanced SLIT2 staining, indicating that SLIT2 was derived from the local hepatocytes but not tumor cells (Figure 3a-3b), which was further confirmed by co-staining of SLIT2 and albumin in both mice or human derived tissues (Figure 3c-3d).

It has been demonstrated that aberrant high expression of SLIT2 could participate the co-evolution of hepatocyte-tumor cells in liver metastasis progress. The roundabout guidance (ROBO) family, except ROBO4, was considered as the most predominant receptor of SLIT2. We further discovered that it was

ROBO1, but not ROBO2 or ROBO3, mainly expressed in metastatic CK19⁺ PDAC cells (Figure 3e, Extended Data Figure 3d). Interestingly, we have discovered that much more ROBO1 positive metastatic niches could be detected in SLIT2 enriched metastasized livers of KPC mice and strong correlation existed between these two molecules in livers bearing metastasis (Figure 3f-3g). What's more, we have analyzed the expression of ROBO1 and SLIT2 in our own datasets containing 14 cases liver metastasis tissues of PDAC patients (OEP000481 in National Omics Data Encyclopedia, NODE) and GEO DataSets (GSE151580 and GSE71729) and the results have revealed strong correlation between these two molecules in liver metastasis which further emphasized the vital role of SLIT2-ROBO1 in liver metastasis progress (Extended Data Figure 3e-3g).

To comprehensively analyze the relationship of prognosis and the expressions of these two molecules, we examined the functions of SLIT2-ROBO1 in primary PDAC via evaluating prognosis of 266 patients. To our interest, we have discovered that high level of ROBO1 would lead to poor prognosis in SLIT2-rich TME; while the results would be just the contrary if TME SLIT2 was deficient (Figure 3h-3i). These prognosis data have deciphered that this axis would be of value for further study.

Taken together, results above have revealed that hepatocytes could upregulate SLIT2 secretion for recruitment and aggregation of ROBO1 positive tumor cells, which could be responsible for co-evolution of them.

SLIT2-ROBO1 mediated co-evolution facilitates outgrowth of liver metastatic niches in vivo

We next generated *Slit2* hepatocytes-specific conditional knockout mice (*Slit2^{fl/fl}/Alb-Cre*, CKO). To rescue, lentivirus carrying loxp-*Slit2* was used to specifically express SLIT2 in hepatocytes which was administrated 14 days before modeling (CKO-RE) (Extended Data Figure 4a-4b). To study the role of SLIT2-ROBO1 interaction in co-evolution of PDAC liver metastasis, tumor cells expressing full-length protein of ROBO1 (Kpc1199 *Robo1-FL* or Panc02 *Robo1-FL*) were intrasplenically implanted into *Slit2^{fl/fl}* (CTRL), CKO and CKO-RE mice respectively (Figure 4a; Extended Data Figure 4b-4d, Figure 5a). The results illustrated that there were much less metastatic colonies in CKO group than those in CTRL group. While in CKO-RE group, the resumption of paracrine of SLIT2 by hepatocytes restored the outgrowth ability of *Robo1-FL* expressed tumor cells (Figure 4b-4c; Extended Data Figure 4e-4h, Figure 5b-5e). Furthermore, tissues of CKO exhibited smaller metastatic niches and less Ki67 staining than those of CTRL or CKO-RE (Extended Data Figure 4h-4k, 5e-5h). To our interest, tumor cells expressing *Robo1-FL* showed serve apoptosis when lacking SLIT2 in the microenvironment. To hamper the direct interaction of SLIT2 and ROBO1, we produced ROBO1 neutralizing antibody specifically targeting the Ig1-Ig2 domain (Figure 4d; Extended Data Figure 4c, Figure 6c). The results revealed that administration of neutralizing antibody sufficiently retarded the progress of metastasis of *Robo1-FL* expressed tumor cells (Figure 4e, Extended Data Figure 6b-6e). Further analyses demonstrated that antibody administration significantly reduced the proliferation and increased apoptosis of metastasized PDAC cells (Extended Data Figure 6f-6g).

To gain the direct evidence that SLIT2-ROBO1 mediated the co-evolution progress, we performed antibody treatment on KPC mice. In this model, high frequency of spontaneous liver MMN occurrence was observed at approximate 15-16 weeks old of mice. To prohibit the formation of PMN in liver, we thus started antibody administration from week12 (Figure 4f). Data has demonstrated that antibody treatment significantly hampered the outgrowth of metastatic niches in left lobules and decreased the percent of ROBO1⁺ PDAC cells in niches (Figure 4g-4i). Interestingly, the accumulation of SLIT2 in adjacent hepatocytes significantly attenuated, indicating that disturbing ROBO1 function in this axis would also significantly affect SLIT2 expression. Furthermore, it was more effective to perform treatment from PMN rather than MMN, since the early administration would prevent more micro niches ($\leq 500\mu\text{m}$) formation in liver (Figure 4k-4l). Meanwhile, the interference of co-evolution loop could be of better efficiency when antibody was administrated from PMN to inhibit SLIT2 expression (Figure 4m).

These results have pointed out the significance of SLIT2-ROBO1 axis in liver metastasis, while the role it played in co-evolution need to be further investigated.

SLIT2-ROBO1 axis is critical for co-evolution between hepatocytes and tumor cells in liver metastasis progress

We then performed IHC-P staining of ROBO1 on 35 cases PDAC liver metastasis tissues with their matched primary tumors. Results have illustrated high ROBO1 expression in most liver metastasis tissues, even if the positive rate of which was much lower in matched primary tumors respectively (Figure 5a-5b). Further results in KPC mice have also confirmed the conclusion (Extended Data Figure 7a). To explore why ROBO1 enriched at liver metastasis and how SLIT2-ROBO1 manipulated the selection of tumor cells in co-evolution, we next performed cell mixture composed of Panc02^{Robo1-FL} and Panc02^{CTRL} each half (PG0) in intrasplenic injection mouse model. Tumor cells derived from separated liver metastasis formed by PG0 were then cultured (PG1) before next modeling and PG2 cells were gained from separated liver metastasis formed by PG1 (Figure 5c). Flow cytometry analysis have demonstrated the increasing of Panc02^{Robo1-FL} cells in population from PG0 to PG2 in tumor cell mixture, indicating that ROBO1 has facilitated survival and outgrowth ability of tumor cells for selection in liver (Figure 5d-5e). To explore whether SLIT2 exerted the driving power, we analyzed the protein levels of ROBO1 and SLIT2 in PMN and MMN of mouse models experienced intrasplenic injection of PG0 and PG1 respectively via IHC-P. The results have revealed that ROBO1 staining at MMN was much stronger in PG1 than those in PG0, while SLIT2 staining could be detected in all groups, displaying an increasing manner from PMN of PG0 to MMN of PG1 (Figure 5f; Extended Data Figure 7b). WB on PG1 and PG2 cells have also provided evidence (Extended Data Figure 7c). Especially, this co-evolution effect could also be disturbed by antibody treatment (Figure 5g). Blocking of SLIT2 and ROBO1 interaction significantly attenuated the staining of both these two molecules (Figure 5h). These data indicated that DTCs-induced SLIT2-rich microenvironment exerted selective pressure on DTCs themselves and provides ROBO1⁺ ones with a growth advantage in liver thus fulfills the co-evolution. To consolidate, another tumor cell mixture Kpc1199^{Mix-1} containing equal amounts of Kpc1199^{Robo1-FL/GFP} and Kpc1199 ^{Δ Robo1/mCherry} or

Kpc1199^{Mix-II} containing equal amounts of Kpc1199^{Robo1-FL/GFP} and Kpc1199^{CTRL/mCherry} were utilized on *Slit2/CKO* or WT mice modeling (Figure 5i). In WT mice, ROBO1-FL expressed tumor cells displayed predominant population in liver metastatic niches especially in Kpc1199^{Mix-I} modeled ones during co-evolution with hepatocytes; while in *Slit2/CKO* mice Kpc1199^{CTRL} cells outcompeted Kpc1199^{Robo1-FL} in absence of SLIT2 (Figure 5j-5k). What's more, the outgrowth of both Kpc1199^{Robo1-FL} cells and Kpc1199^{ΔRobo1} cells were significantly hampered in SLIT2-deficient TME. Data gained from flow cytometry analysis were also in consistence with the results before (Figure 5l; Extended Data Figure 7d).

These phenomena have indicated that ROBO-FL expressed tumor cells and SLIT2 expressed hepatocytes could achieve co-evolution, losing SLIT2 in TME or blocking ROBO1 not only led to failure of ROBO1⁺ tumor cells in competition, but led to their elimination in liver.

ROBO1 acts as a DR to exert dual effects on tumor cells

Previous studies have demonstrated that several receptors of axon guidance family including DCC, Plexin-D1, UNC5 or EphA4 were DRs^{10, 12, 25-26}. Our clinical prognosis data also provided evidence to support that ROBO1 might own dual functions in PDAC progress (Figure 3i-3k)

To confirm, we constructed *Robo1* lacking first two Ig domains ($\Delta Robo1$), which was required for SLIT2 and ROBO1 interaction (Extended Data Figure 4c-4d)²⁷⁻²⁸. Then tumor cells expressing *Robo1-FL* or $\Delta Robo1$ were intrasplenically injected into mice for further investigating the role of ROBO1 on liver metastasis (Figure 6a; Extended Data Figure 8a, Figure 9a). The results showed that mice bearing Kpc1199^{Robo1-FL} or Panc02^{Robo1-FL} injection exhibited more severe liver metastasis compared to that of Kpc1199^{ΔRobo1} or Panc02^{ΔRobo1} group or CTRL group respectively (Figure 6b-6c, Extended Data Figure 8b-8d, Figure 9b-9d). Interestingly, $\Delta Robo1$ expressed tumor cells led to much less metastasis than the other two groups did and induced most apoptosis in metastatic area among three groups (Extended Data Figure 8e-8h, Figure 9e-9h). Survival analysis on these mice were of accordance with the results we gained before (Figure 6d-6e).

Based on the results above, we postulated that ROBO1 might belong to DRs. Examinations of the SLIT2 and ROBO1 expression levels in 10 pancreatic cancer cell lines have elucidated that SLIT2 seldom displayed high expression in PDAC cell lines, especially in liver metastasis-derived CAPAN-1 and cFPAC-1 cells with relatively higher ROBO1 expression (Extended Data Figure 10a-10b). SW-1990 with dual low expressions of ROBO1 and SLIT2 was selected out to transfected with $\Delta ROBO1$, *ROBO1-FL* or empty vector respectively for further study. Results have revealed that proliferation capability of SW-1990^{ROBO1-FL} was much higher than that of SW-1990^{ΔROBO1} when additional recombinant SLIT2 (rSLIT2) existed. Notably, in absence of rSLIT2, both of two groups presented slower growth rate than that of SW-1990^{CTRL} (Figure 6f). Similar results were also obtained in Panc02 (Extended Data Figure 10c). Moreover, the promoting effects of rSLIT2 on PDAC cell growth could be abolished by either neutralizing antibody for rSLIT2 or sROBO, a soluble peptide contained the first 2 Ig domains as a ligand-binding trap, in both SW-1990 and Panc02 (Figure 6g; Extended Data Figure 4C, Figure 10d-10g). Colony formation assay of

either human SW-1990 or murine Panc02 or Kpc1199 also led to the same results (Figure 6h, Extended Data Figure 11a-11e). On the other hand, knockdown of ROBO1 significantly abrogated the growth advantage of PANC-1 and BxPC-3 with dual high expressions of ROBO1 and SLIT2 (Extended Data Figure 11f). While, cell lines with seldom expressed ROBO1 or SLIT2 displayed insensitivity to shROBO1 administration on cell growth (Extended Data Figure 11g-11h). Furthermore, the tumor burden of PANC-1 in subcutaneous xenograft model significantly reduced after stable knockdown of ROBO1 (Figure 6i, Extended Data Figure 11i-11j). Consistently, overexpression of SLIT2 in CAPAN-1, derived from human PDAC liver metastasis, with high level of ROBO1, increased tumor burden (Figure j, Extended Data Figure 11k-11m).

We have also certified cell apoptosis brought by ROBO1 without SLIT2 binding. Flow cytometry analysis showed that both Δ ROBO1 and ROBO1-FL significantly induced cell apoptosis of SW-1990 cells in the absence of SLIT2, while the apoptosis of SW-1990^{ROBO1-FL} was reversed by rSLIT2 at a concentration of 10nM or 30nM, but the apoptosis of SW-1990 ^{Δ ROBO1} could not be reversed (Figure 6k, Extended Data Figure 12a). Similar results could also be obtained by TUNEL assay. Moreover, the sROBO abolished the anti-apoptotic function of rSLIT2 in ROBO1-FL expressed SW-1990 (Figure 6l, Extended Data Figure 12b-12c). Further studies with anti-cleaved caspase3 immunofluorescence, caspase3/7 kit, and western blot all revealed that overexpressing Δ ROBO1 or ROBO1-FL would lead to cell death through triggering caspase-dependent apoptosis via caspase-3, caspase-7, caspase-9, but not caspase-8 in absence of SLIT2 (Figure 6m, Figure S12d). Further *in vivo* experiments also illustrated that ROBO1 in absence of SLIT2 significantly reduced the tumor burden of SW-1990 in subcutaneous PDAC xenograft mice (Figure 6n, Extended Data Figure 12e-12f). Especially, IF displayed that Δ ROBO1 expressed SW-1990 triggered more severe apoptosis than that in subcutaneous tumors of other two groups (Extended Data Figure 12g-12i).

Taken together, these data indicated that ROBO1, recognizing as a DR, would lead to cell apoptosis without ligand binding, while facilitate cell growth when ligands existed. This dual function of ROBO1 mechanically laid foundation for its selective pressure in metastatic tumor-host co-evolution.

Activated ROBO1 facilitates cell growth via enhancing MEK3/6-p38 α MAPK interaction

Given that Mitogen-Activated Protein Kinases (MAPK) pathway controls cell behaviors by modulating cell proliferation, migration, survival and apoptosis, we wondered whether MAPK pathway was involved in SLIT2-ROBO1 axis triggered survival signal for PDAC cell metastasis to liver²⁹⁻³⁰. The results revealed that binding of rSLIT2 to ROBO1-FL significantly induced the phosphorylation of p38 α MAPK while exerted little effects on other key molecules involved in this pathway. Intriguingly, the phosphorylation levels of MEK3 and MEK6, the p38 α MAPK-specific kinases, were also not altered after rSLIT2 stimulation (Extended Data Figure 13a). Furthermore, PH-797804 and VX-702, the specific inhibitors targeting p38 α MAPK, could efficiently abolished the SLIT2-ROBO1 mediated cell growth advantage (Figure 7a, Extended Data Figure b). Additionally, VX-702 efficiently decreased the cell viability of SW-1990^{CTRL} and

rSLIT2 stimulated SW-1990^{ROBO1-FL} to the same level, indicating that the SLIT2-ROBO1 axis induced growth advantage was mediated by p38αMAPK (Figure 7b, Extended Data Figure 13c). Since creative work have been achieved for demonstrating that p38α MAPK was vital in PMN formation and there also has been reported that p38 MAPKs could be rapidly activated by SLIT2-contained conditional medium in 5 min in *Xenopus* retinal growth cones, we hypothesized that p38αMAPK pathway was closely related to SLIT2-ROBO1 mediated co-evolution in PMN and MMN³¹⁻³². Consistent with previous report, our results also showed that 5-10 min treatment of rSLIT2 elevated the phosphorylation level of p38αMAPK and peaked at 30min (Figure 7c). This phenomenon could be observed most obviously in PANC-1 cells with relatively higher expression of ROBO1 (Figure 7d). We further demonstrated that it was ROBO1 that mediated rSLIT2 induced phosphorylation of p38αMAPK in SW-1990^{ROBO1-FL} (Figure 7e). IF staining was also performed to further confirm the increase of P-p38 and nuclear translocation induced by rSLIT2 (Figure 7f, Extended Data Figure 13d), while the level of P-MEK3/6 almost unchanged as before (Figure 7C-7D, Extended Data Figure 13d). Furthermore, patient derived metastasized liver specimens were used for IHC-P staining of P-p38 and the results illustrated that tumor cells with activated P-p38 were surrounded by abundance of SLIT2 (Extended Data Figure 13e). We then proceeded to further seek for the direct evidence that p38αMAPK was phosphorylated in the presence of SLIT2 by *ex vivo* test. The mouse livers metastasized by Panc02^{Robo1-FL} were separated and sliced into two pieces for exposure in medium with or without rSLIT2 exposure for 1 hour respectively. The results displayed that the more significant phosphorylation of p38αMAPK and nuclear accumulation was observed in rSLIT2 treated group than those in control group (Figure 7G, Extended Data Figure 13f). Moreover, livers bearing metastasis of KPC mice were also performed *ex vivo*, data have elucidated that neutralizing antibody against ROBO1 could sufficiently prevent p38αMAPK from phosphorylation and nuclear translocation (Fig. 4H; Extended Data Figure 13g).

Together, these data indicated that the phosphorylation of p38α MAPK triggered by SLIT2-ROBO1 was rapid and less sensitive to alteration of MEK3/6, which inspired us to speculate that there could be direct interactions between activated ROBO1 and p38α MAPK or MEK3/6. The Co-IP elucidated that ROBO1 performed directly binding of p38αMAPK and MEK3/6 (Figure 7i-7j). And further study confirmed that binding of SLIT2 enhanced the phosphorylation of p38αMAPK precipitated by ROBO1 (Figure 7k). Together, these results have elucidated that SLIT2 bound ROBO1 could increase the opportunity for interaction of p38αMAPK and its kinase MEK3/6 to activated the downstream pathway.

Our study has unveiled a novel mechanism of “seed” and “soil” co-evolution, which was driven and pushed forward by DR derived selection pressure through p38αMAPK pathway (Figure 7l).

Discussion

Numerous DTCs derived from primary tumors were released into circulations as “seeds” for distant metastasis, while only few of them achieved MMN in target organs. It is also confusing that why different kinds of tumor cells prefer specific target organs⁵. It is reasonable to gain the explanation that DTCs and

the “soil” (native microenvironment at target organ) can fulfill running-in for reciprocal TMN formation. The necessities involved in this progress are alterability of TMN cells and adaptability of DTCs. In our study, we have unveiled that hepatocytes would provide SLIT2 for PMN formation for only ROBO1 positive PDAC DTCs, supporting the survival of which at their arrival. The implantation and outgrowth of metastatic niches also stimulated more hepatocytes for sustained supplement of SLIT2.

PMNs are built up by aberrantly activated native cells such as tumor associated macrophages (TAMs), cancer associated fibroblasts (CAFs) or some organ specific cells like hepatocytes^{16, 22, 33–35}. These PMN cells exerts metastasis-friendly effects mainly by producing extracellular matrix (ECM) proteins to form niches for DTCs. PMNs are lacking well-established definitive detecting means since they usually generate without histological alteration, and different cancers or different distant metastasis formed by same cancers always requires for different PMN proteins⁵. It is also difficult to gain clinical samples containing PMNs due to the reasons mentioned before: for example, it is often possible that PDAC patients bearing hepatic PMNs may own seemingly healthy liver diagnosed by known tests. While intrasplenic injection mouse models could generate liver metastasis at relative permeant time points once other experiment conditions (e.g. kinds and amounts of injected tumor cells) are kept stable, it is possible for us to decide the approximate time point of PMN. Moreover, we performed examinations on tissues via utilizing reported PMN markers to ensure reliability before further explorations were kept on. We finally filtered out that hepatocytes derived *Slit2*, members of AG family, enriched at PMN and MMN for tumor cells to loom large.

Receptors have long been defined as switches which could fulfil their functions only if triggered by their ligands. While DRs could generate and conducts contrary signals according to the presence or absence of their own ligands¹¹. Furthermore, it is also interesting to discover that many known DRs are encode by neuroendocrine or development related genes and share some common characteristics including that their ligands are usually only abundant in specific organs^{10, 12, 26, 36}. Hypothesis postulates that DRs which are regarded as important guardians of tissue homeostasis perform as safe lock against heterogenous cell implantation including cancer metastasis to other organs¹¹. In normal conditions, DRs are used to restrict cells in the given organ with abundant ligands and prevent cell outgrow into alien microenvironment without ligand by inducing cell apoptosis. As to pathological settings such as metastatic cancers, it is vital for DRs to cause suppressive effects on tumor cells to inhibit metastasis. Here we have uncovered that PDAC tumor cells just utilized this mechanism for their colonization and outgrowth in liver by inducing hepatocytes to secrete SLIT2 from PMN to MMN of liver metastasis. Metastasis requires for changes of both “seed” and “soil” to cater to needs of each other and erases unqualified ones, termed as co-evolution. In this study we tried to explain that the selective power or driving power involved in co-evolution was brought in by the DR properties of ROBO1. SLIT2-rich liver microenvironment not only supported survival and outgrowth of disseminated ROBO1⁺ tumor cells, but also exerted selective pressure on DTCs to enrich ROBO1⁺ cells.

Furthermore, antibody against the SLIT2-ROBO1 axis has provided superior therapeutic effect, since blocking of SLIT2 binding to ROBO1 not only hampered the proliferation advantage brought by ROBO1-p38MAPK pathway, but also triggered ROBO1 induced cell apoptosis, indicating the therapeutic strategy involving DRs might be of potential prospect. Considering that surgery could not be executed on PDAC patients bearing liver metastasis which limits effective treatment, our study has proposed a promising treatment strategy for these cases by targeting SLIT2-ROBO1 axis. For further study, it would be interesting to explore whether this is a common mechanism for cancer metastasis.

Materials And Methods

Constructs & Reagents.

The following antibodies were purchased from Abcam: ROBO1(C-terminal) (ab7279), SLIT2(ab134166), ROBO2(ab75014), ROBO3(ab77216), TIMP1 (ab109125), LOX (ab174316), MIF (ab7027), SAA1/2 (ab199030), CD163 (ab182422), CD68 (ab955), CD11b (ab133357), Ly-6G (ab25377), Keratin19 (Rabbit-derived) (ab52625), Keratin19 (Mouse-derived) (ab7754), P-p38(T180+Y182) (ab4822), P-MEK3(S189/T193)+P-MEK6(S207/T211) (ab4759), MEK3+MEK6 (ab200831), active Caspase 3 (ab2302), Albumin (ab207327), Donkey Anti-Goat IgG H&L (HRP) (ab6885), Rabbit IgG (ab172730). The following antibodies were purchased from Cell Signaling Technology: DAPK1(3008), active Caspase 7 (9491), active Caspase 8 (9748), JNK (9252), P-JNK (Thr183/Tyr185) (9251), ERK1/2 (4695), P-ERK1/2(T202/Y204) (4370), c-jun (9165), P-c-jun (9261), GSK3 α / β (5676), P-GSK3 α / β (Y216/Y279), Mouse IgG (37988). P38 α MAPK antibody (orb229976) was purchased from Biorbyt. Neutralizing antibody towards Ig1-Ig2 domain of ROBO1, HAM1H6-1-8 was purchased from HuaBio. Duolink[®] proximity ligation assay (Olink Bioscience, DUO92007) kit and polybrene (H9268) were purchased from Sigma-Aldrich. P38 α MAPK specific inhibitors VX-702 (S6005) and PH-797804 (S2726) were purchased from Selleck. Cell Counting Kit-8 (CCK-8) was purchased from Dojindo Molecular Technologies. Caspase-3/7 activity Kit (G7790), D-luciferin (P1043) and FuGENE transfection reagent were purchased from Promega. Puromycin (A1113802) was purchased from Gibco. Lipofectamine 2000 was purchased from Invitrogen. G-Dynabeads (10004D) was purchased from Life technologies. Cell Lysis Buffer for Western and IP (P70100) was purchased from New Cell & Molecular Biotech. In Situ Cell Death Fluorescein Kit Tunel (11684795910) and SYBR Premix Ex Taq (04,913,914,001) were purchased from Roche. Trizol reagent (9109) and PrimeScript RT-PCR kit (RR037A) were purchased from Takara. Tumor dissociation kit (mouse) (130-096-730) was purchased from Mlitenyi Biotec.

Clinical samples

Specimens involved in this study mainly included 3 cohorts for respective experimental designs: Cohort I containing 35 cases liver metastasis tissues of PDAC patients together with paired primary tumor tissues was used for IHC-P or IF analysis; cohort II containing 14 fresh cases liver metastasis tissues of PDAC patients together with their paired primary tumor tissues was used for transcriptional analysis, which

could be referred on <https://www.biosino.org/node/project/detail/OEP000481>; cohort III containing 266 cases PDAC primary tumor tissue of patients with their respective prognosis was performed for IHC-P and survival analysis.

Specimens of patients involved in our study were all from – hospital, — University School of Medicine. Specimen collection, experiments design and performance were all approved by local ethics committee in — Hospital with patients' informed consents. All these patients were diagnosed by both clinical surgeons and professional pathologists. Approval letter of — University School of Medicine, — Hospital Ethics Committee is —.

Animal Experiments

lox-stop-lox-Kras^{G12D/+}; *lox-stop-lox-Trp53*^{R172H/+}; *Pdx1-Cre* mice were purchased from The Jackson Laboratories (Bar Harbor, ME) to generate transgenic PDAC mouse model. *Slit2*^{fl/fl} mice and *Alb1-Cre* mice were purchased from Cyagen. All mice above were on the C57BL/6 genetic background. All C57BL/6 wildtype mice and nu/nu mice were purchased from — University.

Animal experiments were approved by Institutional Animal Care and Use Committee of — University. All animals received humane care according to the criteria outlined in the “Guide for the Care and Use of Laboratory Animals” prepared by the National Academy of Sciences and published by the National Institutes of Health. All manipulations were performed under approved protocol number — assigned by the Research Ethics Committee of — University. Mice were housed under specific pathogen-free conditions at — University. We chose male animals at ages of 6 to 8 weeks for tumor studies. Assignment of experimental groups was according to body weights of animals using stratified randomization. Investigators in these animal experiments were blinded to allocation during experiments and outcome assessments.

Liver Metastasis Model and Definition of PMN and MMN.

Intrasplenic injection model provides repeatable and controllable liver metastasis at relative fixed time in mice, which make it possible for research on PMN and MMN^{37–38}. The disadvantages of this model involves that the progress of liver metastasis is more rapid than that in spontaneous ones such as KPC model, while it generates liver metastasis at a stable location and time point once using same experimental conditions¹⁵.

To start, we first explored the time points at which MMN formed in most modeled mice using Kpc1199 cells or Panc02 cells at different concentrations through IHC-P on liver left lobule sections every 3 days. We then chose Kpc1199 at 4×10^5 /mouse or Panc02 1×10^6 /mouse to ensure that the formation of MMN would not be too early or late which would make it difficult to settle down the time points of PMN. Results of IHC-P and CT combined 3D organ reconstruction bioluminescence imaging have finally defined the approximate time point of MMN (day 12- for Kpc1199 and day 9- for Panc02). In preliminary data involved in 50 mice for each cell line respectively, more than 90% mice would generate MMN on right

time (98% for Kpc1199 cells on day 12 and 92% for Panc02 cells on day 9). Then we examined liver sections before MMN formation by staining GFP and reported PMN markers including LOX, TIMP-1, MIF, SAA1/2, and markers of M2 type macrophages. PMN recognized as GFP⁻/markers⁺ liver sections were then determined (day 7-11 for Kpc1199 and day 5-8 for Panc02). In preliminary data involved in 50 mice for each cell line respectively, more than 85% mice would generate PMN on right time according to markers mentioned before (90% for Kpc1199 cells on day 8 and 86% for Panc02 cells on day 6). We thus recognized the time point of both these events (Fig. 1b; Extended Data Fig. 1a).

In brief, 4×10^5 Kpc1199 cells or 1×10^6 Panc02 cells suspended in 20 μ l DMEM without FBS were performed. Immunocompetent isogenic C57BL/6 mice under 2.5% isoflurane inhalation anesthesia were performed 10-15 mm subcostal incision through abdomen skin and peritoneum for surgical exposure of spleen after sterilization. The speed of injection was slower than 5 μ l/s followed by 2s needle retention to prevent leakage. Wound closure was then rapidly performed.

For retrieval of expression of SLIT2 in SLIT2 conditional knockout mice, we perform vector GV348 (Ubi-MCS-SV40-puromycin) containing loxp-NM_004787-loxp for lentivirus package. 200 μ l saline with or without a dose of 3×10^7 of HIV were then delivered into the tail vein of mice respectively. Mice were anesthetized with 2.5% vaporized inhaled isoflurane and placed in restraint that positioned the mouse tail in a lighted, heated groove. The speed of injection was slower than 50 μ l/s. The efficiency of restoration was evaluated 10 days later and the performance. Treatment was performed 2 weeks before the intrasplenic injection of tumor cells. For neutralizing antibody treatment, antibody towards Ig1-Ig2 domain of ROBO1 was performed intraperitoneal injection 1 week before hepatic metastasis modeling, and the administration of which was every 3 days until the mice were sacrificed. For administration of neutralizing antibody on KPC mice, intraperitoneal injection was performed every 3 day since week 12 or week 16 till week 18 before tissue harvesting.

Subcutaneous Xenograft Model.

Athymic male nu/nu mice ages 6 to 8 weeks were used in subcutaneous xenograft model. For SW-1990, SW-1990^{CTRL}, SW-1990 ^{Δ ROBO1} and SW-1990^{ROBO1-FL} suspended in DMEM at a concentration of 1×10^7 cells/ml were injected, the injecting volume was 200 μ l, respectively, and tumor diameters were monitored with calipers every 4 days until the sacrifice of mice at day 24; for CAPAN-1, CAPAN-1^{CTRL} and CAPAN-1^{SLIT2-oe} suspended in DMEM at a concentration of 1×10^7 cells/ml were injected, the injecting volume was 150 μ l, respectively, and tumor diameters were monitored with calipers every 3 days until the sacrifice of mice at day 15; for PANC-1, PANC-1^{shCTRL} and PANC-1^{shROBO1} suspended in DMEM at a concentration of 2×10^7 cells/ml were injected, the injecting volume was 200 μ l, and tumor diameters were monitored with calipers every 5 days until the sacrifice of mice at day 40. Inoculation was performed under the right inguinal skin of mice. Tumor volumes were calculated as volume = $0.5 \times \text{length} \times \text{width}^2$. After mice were sacrificed, the tumors were separated from body and the weights of which were measured.

CT combined 3D Organ Reconstruction Bioluminescence Imaging.

Mice bearing hepatic metastasis composed of luciferase expressing tumor cells were intraperitoneal injected 150 mg D-luciferin at volume of 200 μ l. Mice were then anesthetized with 2.5% vaporized inhaled isoflurane 2 min after injection before placed into IVIS Spectrum (Caliper Life Sciences, Waltham, MA). CT was then performed to merge with firefly bioluminescence signals. For organ reconstruction, CT image was utilized to be placed into auto-reconstructed liver and spleen at opacity of 20%. The normalization and quantification of firefly bioluminescence signals were performed according to the red cube surrounding area. Mice were sacrificed at the end of test, the tumor-bearing livers were immediately isolated before icy PBS washing. Photo of luciferin emission imaging of every liver was then taken. All the imaging or calculating were performed by living Image software, version 4.5.3.

Transcriptional Analysis

Panc02 or Kpc1199 intrasplenically injected mouse models were performed. Then mice were sacrificed at specific days and the livers of which were harvested. For Panc02 modeled mice, the time points were day 3, day 6 and day12; for Kpc1199 modeled ones, the time points were day 3, day8 and day15. The fresh livers gained were then washed by icy saline and left hepatic lobules of which were sliced into 2 \times 2 \times 2 mm³ cubes. Especially, for tissues of Panc02 modeled mice on day12 and Kpc1199 modeled mice on day 15, obvious metastatic niches could be observed, while only adjacent livers without metastasis would be selected for further study. In the following-up, PMN and MMN markers were measured before transcriptional analysis. The analysis data is available in the Sequence Read Archive (SRA), the number of which is PRJNA590588 (for Kpc1199) and PRJNA590599 (for Panc02).

For GSEA, 4GB (64bit) GSEA v4.01 Java Web Start (all platforms) were used. Analyses were performed as D3 vs. D8 and D3 vs. D15 for Kpc1199 and D3 vs. D6 and D3 vs. D12 for Panc02. Gene sets involved in these analyses were "c2.cp.kegg.v7.0.symbols.gmt".

Metastatic Tumor Dissociation, Culture and Examination Intrasplenic injection model mice bearing liver metastasis were sacrificed after operation. The metastasized livers were then gained carefully and immediately followed by icy saline washing. Metastatic niches were carefully recognized and separated from liver. Fine-pointed forceps were used for detachment of remained liver parenchymal tissue, tumor associated fibrous or necrotic areas. Then "clean" liver metastatic tumors were washed by icy DMEM for 3 times and cut into 1 \times 1 \times 1mm cubes before transferred into 2.5 mL DMEM containing 100 μ L of Enzyme D, 50 μ L of Enzyme R, and 12.5 μ L of Enzyme A provided in kit. After suspending the dissociated tumor tissues in the solution mentioned before, the tubes were tightly closed and put on constant temperature oscillator for 1h at 37 $^{\circ}$ C, 120 rpm. The mixtures were then performed centrifugation at 1000 rpm for 5 min and the samples would be resuspended in DMEM for 3 times. The suspended tumor cells in DEMN were next for cell counting before planted on dishes. Briefly, approximate 5 \times 10⁴ cells in complete DMEM would be add into 6-hole plates for further culture. Examination of GFP or mCherry expression and activity of luciferase would be taken into consideration for tumor cell certification.

Histology and Immunohistochemistry.

The tissues were fixed in 4% paraformaldehyde and embedded in paraffinized blocks. The blocks were cut into sections at a thickness of 5 μm , then deparaffinized and rehydrated for histopathological evaluation. For hematoxylin-eosin (HE) staining, the sections were dyed in hematoxylin for 5 mins and in eosin for 5-10 secs for HE staining. For immunohistochemical staining, the sections were placed in sodium citrate buffer solution (PH 6.0) for 20 minutes to carry out repair of tissue antigens. Then these sections were incubated with 0.3% hydrogen peroxide/phosphate-buffered saline for 30 mins and blocked with 10% (w/v) BSA (Sangon)/Phosphate-buffered saline (PBS). Slides were first incubated using the antibodies at 4°C overnight with optimal dilution. After washed three times with 1×PBS, the slides were labeled by HRP second antibody at room temperature for 1 h. Then the sections were washed three times in 1×PBS, then treated with DAB substrate liquid (Thermo) and counterstained by hematoxylin. All the sections were observed and photographed with a microscope (Carl Zeiss). Various primary antibodies were used as follow: ROBO1 (N-Terminal) (1:300), ROBO2(1:300), ROBO3 (1:500), SLIT2 (1:500), CK19 (1:500), p38 α (1:700), P-p38(T180+Y182) (1:500), F4/80 (1:200), CD68 (1:100), CD11b (1:200), Ly-6G (1:300), LOX (1:500), MIF (1:300), TIMP-1 (1:500), SAA1/2 (1:700). Secondary antibodies were utilized as follow: HRP-conjugated anti-Goat (1:1000), HRP- conjugated anti-Rabbit (1:500), HRP- conjugated anti-Mouse (1:500).

Immunofluorescence Staining.

For tissue staining, the sections carried tissues were placed in PH 6.0 sodium citrate buffer solution for 20 minutes to subject heat-mediated antigen retrieval. Then these sections were blocked by 10% (w/v) BSA/PBS and co-incubated with primary antibodies at 4°C overnight with optimal dilution. For cell staining, SW1990 cells at 2×10^4 cells per well, PANC1 at 2×10^4 per well or MIA PaCa-2 at 3×10^4 cells per well were seeded on slides in 12-well plates (ibidi) respectively and cultured at 37°C. After washed three times with 1×PBS, the slides were labeled with Alexa Fluor 594-conjugated anti-rabbit antibody and Fluor 488 conjugated anti-mouse antibody at room temperature for 1 h. The nucleus was stained with DAPI (Sigma) after the redundant second antibody were removed. After washed three times with 1×PBS, the immunofluorescence signals were captured using confocal-scropy (Carl Zeiss).

Ex vivo Living Tumor Tissue Culture

Liver tissues containing Panc02 ^{Robo1-FL} formed metastatic niches gained from intrasplenic injection mouse model or metastasized liver tissue of KPC mouse model were separated on ice for maintaining their structural integrity and activity. Then tissues were washed in icy saline within 15min after resection, followed by sliced into small cubes at an approximate volume of $5 \times 5 \times 5 \text{ mm}^3$. Each cube must contain liver metastatic niches and their adjacent livers. Then these cubes were placed into complete medium with or without 30nM rSLIT2 administration/ ROBO1 neutralizing antibody respectively.

For intrasplenic model derived livers, these tissues were stimulated for 1h to measure the rapid phosphorylation of p38 α MAPK. Importantly, a cube would be cut into two pieces in the middle and placed into medium with or without rSLIT2 respectively for ensuring the same tumor microenvironment (TME) of

metastatic niches undergoing. After rSLIT2 administration, all tissues were immediately fixed by 4% paraformaldehyde for further IHC-P test.

For KPC mice derived livers, these tissues were treated with antibody no more than 8h to maintain the tissue structures. All tissues were then immediately fixed by 4% paraformaldehyde followed by IF staining.

Recombinant SLIT2 and sROBO Protein Expression and Purification

Episomal expression vector with pCEP-Pu-Strep II-tag were cloned in the SLIT2 or sROBO1 ORF. The reconstructed plasmids were transfected into 293T cell line for recombinant protein expression. Puromycin for screening was administrated into complete DMEM at a concentration of 5-10 µg/ml 48h after transfection for 10 days and 2 µg/ml of which was performed to maintain the expression positive cells after that. Then the culture medium of transfected 293T was collected and applied to Strep Tactin sepharose column (IBA, 2-1202-101) followed by washing of binding buffer and elution buffer containing 2.5mM desthiobiotin on ice. The harvested fractions were further quantified by Nanodrop 2000 spectrophotometer (Thermo) and western blotting was performed for identification. See also our pervious study³⁹.

Cell Culture

Human PDAC cell lines PANC-1, BxPC-3, CFPAC-1, HPAC, CAPAN-1, CAPAN-2, Patu 8988, MIA PaCa-2, SW-1990 and AsPC-1 and Murine cell lines Panc02 and Kpc1199 were all preserved in – Hospital, School of Medicine, – University. All cells were cultured in suggested conditions following granted protocols including respective medium supplemented 10% (v/v) FBS and 1% antibiotics and kept in 37°C humidified incubators with 5% CO₂. Medium contained 4.5g/L glucose and 2mM L-glutamine when cellular function assays were performed.

Cell Transfection

For shRNA transfection, lentivirus carried shRNA sequences were in Table. 1

For negative control, scramble shRNA targeting no known genes were also designed and used.

For overexpression, pcDNA3.1-*ROBO1*-FL vector, pcDNA3.1- Δ *ROBO1* vector or pcDNA3.1-*SLIT2* vector were utilized for lentivirus package and transfection. The empty vector was also taken out for negative control.

All transfected cells were screened with puromycin at a concentration gradient of 1µg/ml to 10µg/ml for more than at least 10 days before the transfection efficiencies were evaluated.

Cell Viability Assay.

Cells were seeded into 96-well plates. The numbers of planted cells were as follow: for human cell lines: SW-1990: 3000/well; BxpC-3: 3000/well; PANC-1: 5000/well; CFPAC-1: 6000/well; CAPAN-1: 3000/cell, HPAC: 5000/well; for murine cell lines: Panc02: 3000/well. The measurement or treatment for these cells started after overnight incubation and recognized as day 0. The consistent measurements lasted from day 0 to day 5; for cell stress exertion, culture medium in absence of FBS were performed after day 2. For rSLIT2 treatment, the concentration was 30nM in culture medium. VX-702 treatment was performed at a concentration of 5 μ M for normal cell viability assay and a concentration gradient of 200nM, 1 μ M, 5 μ M, 25 μ M, 125 μ M for concentration dependence test. PH-797804 treatment was performed at a concentration of 50 μ M for normal cell viability assay and a concentration gradient of 80nM, 400nM, 2 μ M, 10 μ M, 50 μ M for concentration dependence test. sROBO was performed at a concentration of 5 μ M in culture medium. At indicated time point, diluted CCK-8 in culture medium at a concentration of 10% (v/v) was added 100 μ l in every well and incubated at 37°C for 1 hour. Cell viability was monitored using Power Wave XS microplate reader (BIO-TEK) by measuring the absorbance at 450nm. Every group contained 5 repeated wells and every experience was performed three times.

Colony Formation Assay

Panc02, Kpc1199 and SW-1990 cell lines cultured at 70% confluence were utilized for colony formation assay to ensure them at phase of logarithmic growth. Cells were detached with 0.25% trypsin/0.01% EDTA and planted in 3mm dishes in complete medium with or without rSLIT2 treatment (10nM or 30nM) respectively for growth. The numbers of planted cells were as follow: SW-1990: 4000/dish; Panc02: 3000/dish; Kpc1199:3000/dish. The medium was changed every 3 days. All cells were then fixed in 4% paraformaldehyde for 30 mins and stained by crystal violet. The measurement of the results was performed by Image J via calculating the pixels of staining area.

Cell Apoptosis Assay

Cell apoptosis measured by Caspase-3/7 Activity Kit: SW-1990^{CTRL}, SW-1990 ^{Δ ROBO1} and SW-1990^{ROBO1-FL} were planted at a concentration of 4000/well into 96-well plates. Serum starvation was performed for 48 hours after 3-day growth with or without 30nM rSLIT2 administration. Then the operation and measurement of the activity of Caspase -3/7 was performed strictly according to manufacturer's guidance.

Cell apoptosis measured by Annexin V & propidium iodide (PI) staining: SW-1990^{CTRL}, SW-1990 ^{Δ ROBO1} and SW-1990^{ROBO1-FL} were detached with 0.25% trypsin/0.01% EDTA in 1 \times PBS after treatment with or without rSLIT2 administration (10nM or 30nM). Then suspended cells were harvested in DMEM and centrifuged at 800rpm for 3 minutes. These cells were then stained with 3.5 μ l Annexin V and 3.5 μ l PI diluted in 100 μ l binding buffer after 1 \times PBS washing. Flow cytometry (BD) was performed to analyze after incubation of cells for 20 minutes at 25°C.

Cell Apoptosis measured by Terminal deoxynucleotidyl transferase (TdT) dUTP nick-end labeling (TUNEL) assay: all steps were strictly conducted in accordance with instructions.

Quantitative Real-time PCR. Total RNA extraction was performed using the Trizol reagent followed by reversely transcription to harvest the cDNA. 7500 Real-time PCR system (Applied Biosystems, USA) was used to performing the qPCR at recommended cycling settings. The conditions were 1 initial cycle at 95°C for 2 min, 35 cycles of 5

sec at 95°C and 31 sec at 60°C. $2^{-\Delta CT}$ method was utilized for evaluating and normalization to 18S mRNA levels when relative mRNA expressions were calculated.

The primers mentioned were listed in Table. 2.

Western Blotting. For cell protein extraction, cells were lysed in lysis buffer contained Cell Lysis Buffer for Western and IP (New Cell & Molecular Biotech; P70100) and Protease and Phosphatase Inhibitor Cocktail (New Cell & Molecular Biotech; P002) on ice for 10 min before centrifuged at 12,000×g for 15 min at 4°C. For tissue protein extraction, tissues were lysed in lysis buffer of volume at 10×weight of tissue(g) ml, which contained NCM RIPA Buffer (New Cell & Molecular Biotech; WB3100) and Protease and Phosphatase Inhibitor Cocktail on ice for 15 min before centrifuged at 13,500×g for 20 min at 4°C. The supernatants were collected, and the protein concentration was measured by BCA Protein Assay Kit (Pierce Biotechnology) followed by standardization. SDS-PAGE Sample Loading Buffer, 5× (Beyotime; P0015) was added before boiling water bath for 10 min. Especially, the cytoplasmic and nuclear protein extraction were performed using NE-PER™ Nuclear and Cytoplasmic Extraction Reagents (Thermo Fisher Scientific) and strictly followed the guidance of product. Protein lysates were separated by 8-12% SDS-PAGE gel electrophoresis followed by transferring onto NC membrane. For normal proteins, skimmed milk powder (Invitrogen) diluted into TBST (containing 1‰ Tween 20) at a concentration of 5% and for phosphorylated proteins, BSA (Sangon) powder diluted into TBST at a concentration of 5% were utilized to perform blockage for 1-2 hour at room temperature. Various primary antibodies were used as follow: ROBO1 (N-Terminal) (1:500), ROBO1 (C-Terminal) (1:1000), SLIT2 (1:1000), ROBO2 (1:1000), ROBO3 (1:500), P-MEK3(S189/T193)+P-MEK6(S207/T211) (1:500), MEK3+MEK6 (1:1000), p38α (1:1000), P-p38(T180+Y182) (1:1000), β-Actin (1:10000), GSK3α/β (1:1000), P-GSK3α/β(Y216/Y279) (1:1000), c-jun (1:1000), P-c-jun(S63) (1:1000), JNK(1:1000), P-JNK (T183/Y185), ERK1/2(1:1000), P-ERK1/2(T202/Y204). Membranes after overnight incubation with primary antibodies diluted into Universal Antibody Diluent (New Cell & Molecular Biotech; WB500D) were probed by secondary antibodies. Secondary antibodies were utilized as follow: HRP-conjugated anti-Goat (1:5000), HRP-conjugated anti-Rabbit (1:1000), HRP- conjugated anti-Mouse (1:1000), Alexa Fluor® 680-conjugated anti-Rabbit (1:15000), Alexa Fluor® 790-conjugated anti-mouse (1:15000). For HRP-conjugated secondary antibody incubated membranes, Lumi Q ECL reagent solution kit (Share-Bio) was performed to detected by ChemiDoc™ XRS+ system (BIO-RAD). The exposure was from 1 s and 1 time per second. For Alexa Flour®-conjugated secondary antibody incubated membranes, bound secondary antibodies were detected by Odyssey imaging system (LI-COR Biosciences, Lincoln, NE).

Dynabead Immunoprecipitation

Primary antibodies or IgG were diluted in 200µl icy PBST (0.02% Tween 20) to the same concentration. 50µl protein G Dynabeads were pre-cleaned and mixed with diluted antibodies or IgG to rotate at room temperature for 25 min. Various primary antibodies were used as follow: ROBO1 (N-Terminal) (1:50), ROBO1 (C-Terminal) (1:100), p38α (1:100), MEK3/6 (1:50).

Cells were lysed in lysis buffer contained Cell Lysis Buffer for Western and IP (New Cell & Molecular Biotech; P70100) and Protease and Phosphatase Inhibitor Cocktail (New Cell & Molecular Biotech; P002) on ice for 10 min before centrifuged at 12,000 rpm for 15 min at 4°C. Then lysates were mixed with antibody-beads at room temperature for 30-60 min followed by immunoblotting assessment.

Statistical Analysis

Software IBM SPSS statistics 19.0 and GraphPad 7.0 were used in this study. Data presented were mean ± S.E.M. Two-tailed Student's t-test was used for evaluation of differences between two groups. For evaluations of cell viability or tumor growth, repeat measure ANOVA was performed.

References

1. Curtis, M.; Kenny, H. A.; Ashcroft, B.; Mukherjee, A.; Johnson, A.; Zhang, Y.; Helou, Y.; Batlle, R.; Liu, X.; Gutierrez, N.; Gao, X.; Yamada, S. D.; Lastra, R.; Montag, A.; Ahsan, N.; Locasale, J. W.; Salomon, A. R.; Nebreda, A. R.; Lengyel, E., Fibroblasts Mobilize Tumor Cell Glycogen to Promote Proliferation and Metastasis. *Cell Metab* 2019, *29* (1), 141-155 e9.
2. Zhang, L.; Zhang, S.; Yao, J.; Lowery, F. J.; Zhang, Q.; Huang, W. C.; Li, P.; Li, M.; Wang, X.; Zhang, C.; Wang, H.; Ellis, K.; Cheerathodi, M.; McCarty, J. H.; Palmieri, D.; Saunus, J.; Lakhani, S.; Huang, S.; Sahin, A. A.; Aldape, K. D.; Steeg, P. S.; Yu, D., Microenvironment-induced PTEN loss by exosomal microRNA primes brain metastasis outgrowth. *Nature* 2015, *527* (7576), 100–104.
3. Paget, S., The distribution of secondary growths in cancer of the breast. 1889. *Cancer Metastasis Rev* 1989, *8* (2), 98–101.
4. Liu, Y.; Cao, X., Characteristics and Significance of the Pre-metastatic Niche. *Cancer Cell* **2016**, *30* (5), 668–681.
5. Peinado, H.; Zhang, H.; Matei, I. R.; Costa-Silva, B.; Hoshino, A.; Rodrigues, G.; Psaila, B.; Kaplan, R. N.; Bromberg, J. F.; Kang, Y.; Bissell, M. J.; Cox, T. R.; Giaccia, A. J.; Ertler, J. T.; Hiratsuka, S.; Ghajar, C. M.; Lyden, D., Pre-metastatic niches: organ-specific homes for metastases. *Nat Rev Cancer* **2017**, *17* (5), 302–317.
6. Zhou, X.; Wahane, S.; Friedl, M. S.; Kluge, M.; Friedel, C. C.; Avrampou, K.; Zachariou, V.; Guo, L.; Zhang, B.; He, X.; Friedel, R. H.; Zou, H., Microglia and macrophages promote corraling, wound compaction and recovery after spinal cord injury via Plexin-B2. *Nat Neurosci* 2020, *23* (3), 337–350.
7. Suter, T.; Jaworski, A., Cell migration and axon guidance at the border between central and peripheral nervous system. *Science* 2019, *365* (6456).

8. Jurcak, N. R.; Rucki, A. A.; Muth, S.; Thompson, E.; Sharma, R.; Ding, D.; Zhu, Q.; Eshleman, J. R.; Anders, R. A.; Jaffee, E. M.; Fujiwara, K.; Zheng, L., Axon Guidance Molecules Promote Perineural Invasion and Metastasis of Orthotopic Pancreatic Tumors in Mice. *Gastroenterology* 2019, *157* (3), 838-850 e6.
9. Biankin, A. V.; Waddell, N.; Kassahn, K. S.; Gingras, M. C.; Muthuswamy, L. B.; Johns, A. L.; Miller, D. K.; Wilson, P. J.; Patch, A. M.; Wu, J.; Chang, D. K.; Cowley, M. J.; Gardiner, B. B.; Song, S.; Harliwong, I.; Idrisoglu, S.; Nourse, C.; Nourbakhsh, E.; Manning, S.; Wani, S.; Gongora, M.; Pajic, M.; Scarlett, C. J.; Gill, A. J.; Pinho, A. V.; Rooman, I.; Anderson, M.; Holmes, O.; Leonard, C.; Taylor, D.; Wood, S.; Xu, Q.; Nones, K.; Fink, J. L.; Christ, A.; Bruxner, T.; Cloonan, N.; Kolle, G.; Newell, F.; Pinese, M.; Mead, R. S.; Humphris, J. L.; Kaplan, W.; Jones, M. D.; Colvin, E. K.; Nagrial, A. M.; Humphrey, E. S.; Chou, A.; Chin, V. T.; Chantrill, L. A.; Mawson, A.; Samra, J. S.; Kench, J. G.; Lovell, J. A.; Daly, R. J.; Merrett, N. D.; Toon, C.; Epari, K.; Nguyen, N. Q.; Barbour, A.; Zeps, N.; Australian Pancreatic Cancer Genome, I.; Kakkar, N.; Zhao, F.; Wu, Y. Q.; Wang, M.; Muzny, D. M.; Fisher, W. E.; Brunicardi, F. C.; Hodges, S. E.; Reid, J. G.; Drummond, J.; Chang, K.; Han, Y.; Lewis, L. R.; Dinh, H.; Buhay, C. J.; Beck, T.; Timms, L.; Sam, M.; Begley, K.; Brown, A.; Pai, D.; Panchal, A.; Buchner, N.; De Borja, R.; Denroche, R. E.; Yung, C. K.; Serra, S.; Onetto, N.; Mukhopadhyay, D.; Tsao, M. S.; Shaw, P. A.; Petersen, G. M.; Gallinger, S.; Hruban, R. H.; Maitra, A.; Iacobuzio-Donahue, C. A.; Schulick, R. D.; Wolfgang, C. L.; Morgan, R. A.; Lawlor, R. T.; Capelli, P.; Corbo, V.; Scardoni, M.; Tortora, G.; Tempero, M. A.; Mann, K. M.; Jenkins, N. A.; Perez-Mancera, P. A.; Adams, D. J.; Largaespada, D. A.; Wessels, L. F.; Rust, A. G.; Stein, L. D.; Tuveson, D. A.; Copeland, N. G.; Musgrove, E. A.; Scarpa, A.; Eshleman, J. R.; Hudson, T. J.; Sutherland, R. L.; Wheeler, D. A.; Pearson, J. V.; McPherson, J. D.; Gibbs, R. A.; Grimmond, S. M., Pancreatic cancer genomes reveal aberrations in axon guidance pathway genes. *Nature* 2012, *491* (7424), 399-405.
10. Luchino, J.; Hocine, M.; Amoureux, M.-C.; Gibert, B.; Bernet, A.; Royet, A.; Treilleux, I.; Lécine, P.; Borg, J.-P.; Mehlen, P., Semaphorin 3E suppresses tumor cell death triggered by the plexin D1 dependence receptor in metastatic breast cancers. *Cancer Cell* 2013, *24* (5), 673–685.
11. Negulescu, A. M.; Mehlen, P., Dependence receptors - the dark side awakens. *FEBS J* 2018, *285* (21), 3909–3924.
12. Grandin, M.; Meier, M.; Delcros, J. G.; Nikodemus, D.; Reuten, R.; Patel, T. R.; Goldschneider, D.; Orriss, G.; Krahn, N.; Boussouar, A., Structural decoding of the Netrin-1/UNC5 interaction and its therapeutical implications in cancers. *Cancer Cell* 2016, *29* (2), 173–185.
13. Genevois, A. L.; Ichim, G.; Coissieux, M. M.; Lambert, M. P.; Laval, F.; Goldschneider, D.; Jarrosson-Wuilleme, L.; Lepinasse, F.; Gouysse, G.; Herceg, Z.; Scoazec, J. Y.; Tauszig-Delamasure, S.; Mehlen, P., Dependence receptor TrkC is a putative colon cancer tumor suppressor. *Proc Natl Acad Sci U S A* 2013, *110* (8), 3017–22.
14. Lim, C.; Cauchy, F.; Azoulay, D.; Farges, O.; Ronot, M.; Pocard, M., Tumour progression and liver regeneration—insights from animal models. *Nat Rev Gastroenterol Hepatol* 2013, *10* (8), 452–62.
15. Little, E. C.; Wang, C.; Watson, P. M.; Watson, D. K.; Cole, D. J.; Camp, E. R., Novel immunocompetent murine models representing advanced local and metastatic pancreatic cancer. *J Surg Res* 2012, *176* (2), 359–66.

16. Seubert, B.; Grünwald, B.; Kobuch, J.; Cui, H.; Schelter, F.; Schaten, S.; Siveke, J. T.; Lim, N. H.; Nagase, H.; Simonavicius, N., Tissue inhibitor of metalloproteinases (TIMP)-1 creates a premetastatic niche in the liver through SDF-1/CXCR4-dependent neutrophil recruitment in mice. *Hepatology* 2015, *61* (1), 238–248.
17. Pommier, A.; Anaparthi, N.; Memos, N.; Kelley, Z. L.; Gouronnec, A.; Yan, R.; Auffray, C.; Albregues, J.; Egeblad, M.; Iacobuzio-Donahue, C. A., Unresolved endoplasmic reticulum stress engenders immune-resistant, latent pancreatic cancer metastases. *Science* 2018, *360* (6394), eaao4908.
18. Cox, T. R.; Rumney, R. M.; Schoof, E. M.; Perryman, L.; Høye, A. M.; Agrawal, A.; Bird, D.; Ab Latif, N.; Forrest, H.; Evans, H. R., The hypoxic cancer secretome induces pre-metastatic bone lesions through lysyl oxidase. *Nature* 2015, *522* (7554), 106.
19. Costa-Silva, B.; Aiello, N. M.; Ocean, A. J.; Singh, S.; Zhang, H.; Thakur, B. K.; Becker, A.; Hoshino, A.; Mark, M. T.; Molina, H., Pancreatic cancer exosomes initiate pre-metastatic niche formation in the liver. *Nature cell biology* 2015, *17* (6), 816.
20. Chu, G. C.-Y.; Zhau, H. E.; Wang, R.; Rogatko, A.; Feng, X.; Zayzafoon, M.; Liu, Y.; Farach-Carson, M. C.; You, S.; Kim, J., RANK-and c-Met-mediated signal network promotes prostate cancer metastatic colonization. *Endocrine-related cancer* 2014, *21* (2), 311–326.
21. Gil-Bernabé, A. M.; Ferjancic, S.; Tlalka, M.; Zhao, L.; Allen, P. D.; Im, J. H.; Watson, K.; Hill, S. A.; Amirkhosravi, A.; Francis, J. L., Recruitment of monocytes/macrophages by tissue factor-mediated coagulation is essential for metastatic cell survival and premetastatic niche establishment in mice. *Blood* 2012, blood-2011-08-376426.
22. Lee, J. W.; Stone, M. L.; Porrett, P. M.; Thomas, S. K.; Komar, C. A.; Li, J. H.; Delman, D.; Graham, K.; Gladney, W. L.; Hua, X.; Black, T. A.; Chien, A. L.; Majmundar, K. S.; Thompson, J. C.; Yee, S. S.; O'Hara, M. H.; Aggarwal, C.; Xin, D.; Shaked, A.; Gao, M.; Liu, D.; Borad, M. J.; Ramanathan, R. K.; Carpenter, E. L.; Ji, A.; de Beer, M. C.; de Beer, F. C.; Webb, N. R.; Beatty, G. L., Hepatocytes direct the formation of a pro-metastatic niche in the liver. *Nature* 2019, *567* (7747), 249–252.
23. Poruk, K. E.; Blackford, A. L.; Weiss, M. J.; Cameron, J. L.; He, J.; Goggins, M.; Rasheed, Z. A.; Wolfgang, C. L.; Wood, L. D., Circulating Tumor Cells Expressing Markers of Tumor-Initiating Cells Predict Poor Survival and Cancer Recurrence in Patients with Pancreatic Ductal Adenocarcinoma. *Clin Cancer Res* 2017, *23* (11), 2681–2690.
24. Poruk, K. E.; Valero, V., 3rd; Saunders, T.; Blackford, A. L.; Griffin, J. F.; Poling, J.; Hruban, R. H.; Anders, R. A.; Herman, J.; Zheng, L.; Rasheed, Z. A.; Laheru, D. A.; Ahuja, N.; Weiss, M. J.; Cameron, J. L.; Goggins, M.; Iacobuzio-Donahue, C. A.; Wood, L. D.; Wolfgang, C. L., Circulating Tumor Cell Phenotype Predicts Recurrence and Survival in Pancreatic Adenocarcinoma. *Ann Surg* 2016, *264* (6), 1073–1081.
25. Mehlen, P.; Rabizadeh, S.; Snipas, S. J.; Assa-Munt, N.; Salvesen, G. S.; Bredesen, D. E., The DCC gene product induces apoptosis by a mechanism requiring receptor proteolysis. *Nature* 1998, *395* (6704), 801–4.

26. Furne, C.; Ricard, J.; Cabrera, J. R.; Pays, L.; Bethea, J. R.; Mehlen, P.; Liebl, D. J., EphrinB3 is an anti-apoptotic ligand that inhibits the dependence receptor functions of EphA4 receptors during adult neurogenesis. *Biochim Biophys Acta* **2009**, *1793* (2), 231–8.
27. Morlot, C.; Thielens, N. M.; Ravelli, R. B.; Hemrika, W.; Romijn, R. A.; Gros, P.; Cusack, S.; McCarthy, A. A., Structural insights into the Slit-Robo complex. *Proceedings of the National Academy of Sciences* **2007**, *104* (38), 14923-14928.
28. Hohenester, E., Structural insight into Slit–Robo signalling. Portland Press Limited: 2008.
29. Sebolt-Leopold, J. S.; Herrera, R., Targeting the mitogen-activated protein kinase cascade to treat cancer. *Nature Reviews Cancer* **2004**, *4* (12), 937.
30. Wagner, E. F.; Nebreda, Á. R., Signal integration by JNK and p38 MAPK pathways in cancer development. *Nature Reviews Cancer* **2009**, *9* (8), 537.
31. Piper, M.; Anderson, R.; Dwivedy, A.; Weinl, C.; Van Horck, F.; Leung, K. M.; Cogill, E.; Holt, C., Signaling mechanisms underlying Slit2-induced collapse of *Xenopus* retinal growth cones. *Neuron* **2006**, *49* (2), 215–228.
32. Gui, J.; Zahedi, F.; Ortiz, A.; Cho, C.; Fuchs, S. Y., Activation of p38 α stress-activated protein kinase drives the formation of the pre-metastatic niche in the lungs. *Nature Cancer* **2020**.
33. Erler, J. T.; Bennewith, K. L.; Cox, T. R.; Lang, G.; Bird, D.; Koong, A.; Le, Q. T.; Giaccia, A. J., Hypoxia-induced lysyl oxidase is a critical mediator of bone marrow cell recruitment to form the premetastatic niche. *Cancer Cell* **2009**, *15* (1), 35–44.
34. Nielsen, S. R.; Quaranta, V.; Linford, A.; Emeagi, P.; Rainer, C.; Santos, A.; Ireland, L.; Sakai, T.; Sakai, K.; Kim, Y.-S.; Engle, D.; Campbell, F.; Palmer, D.; Ko, J. H.; Tuveson, D. A.; Hirsch, E.; Mielgo, A.; Schmid, M. C., Macrophage-secreted granulin supports pancreatic cancer metastasis by inducing liver fibrosis. *Nature cell biology* **2016**, *18* (5), 549–560.
35. Li, Q.; Zhu, C. C.; Ni, B.; Zhang, Z. Z.; Jiang, S. H.; Hu, L. P.; Wang, X.; Zhang, X. X.; Huang, P. Q.; Yang, Q.; Li, J.; Gu, J. R.; Xu, J.; Luo, K. Q.; Zhao, G.; Zhang, Z. G., Lysyl oxidase promotes liver metastasis of gastric cancer via facilitating the reciprocal interactions between tumor cells and cancer associated fibroblasts. *EBioMedicine* **2019**, *49*, 157–171.
36. Delloye-Bourgeois, C.; Gibert, B.; Rama, N.; Delcros, J. G.; Gadot, N.; Scoazec, J. Y.; Krauss, R.; Bernet, A.; Mehlen, P., Sonic Hedgehog promotes tumor cell survival by inhibiting CDON pro-apoptotic activity. *PLoS Biol* **2013**, *11* (8), e1001623.
37. Nielsen, S. R.; Quaranta, V.; Linford, A.; Emeagi, P.; Rainer, C.; Santos, A.; Ireland, L.; Sakai, T.; Sakai, K.; Kim, Y.-S., Macrophage-secreted granulin supports pancreatic cancer metastasis by inducing liver fibrosis. *Nature cell biology* **2016**, *18* (5), 549.
38. Costa-Silva, B.; Aiello, N. M.; Ocean, A. J.; Singh, S.; Zhang, H.; Thakur, B. K.; Becker, A.; Hoshino, A.; Mark, M. T.; Molina, H.; Xiang, J.; Zhang, T.; Theilen, T. M.; Garcia-Santos, G.; Williams, C.; Ararso, Y.; Huang, Y.; Rodrigues, G.; Shen, T. L.; Labori, K. J.; Lothe, I. M.; Kure, E. H.; Hernandez, J.; Doussot, A.; Ebbesen, S. H.; Grandgenett, P. M.; Hollingsworth, M. A.; Jain, M.; Mallya, K.; Batra, S. K.; Jarnagin, W.

- R.; Schwartz, R. E.; Matei, I.; Peinado, H.; Stanger, B. Z.; Bromberg, J.; Lyden, D., Pancreatic cancer exosomes initiate pre-metastatic niche formation in the liver. *Nat Cell Biol* **2015**, *17* (6), 816–26.
39. Zhang, Y. L.; Li, Q.; Yang, X. M.; Fang, F.; Li, J.; Wang, Y. H.; Yang, Q.; Zhu, L.; Nie, H. Z.; Zhang, X. L.; Feng, M. X.; Jiang, S. H.; Tian, G. A.; Hu, L. P.; Lee, H. Y.; Lee, S. J.; Xia, Q.; Zhang, Z. G., SPON2 Promotes M1-like Macrophage Recruitment and Inhibits Hepatocellular Carcinoma Metastasis by Distinct Integrin-Rho GTPase-Hippo Pathways. *Cancer Res* **2018**, *78* (9), 2305–2317.

Tables

Gene	Sequence (5' to 3')
sh <i>ROBO1</i> (NM_002941.4)	GGAGAGAAGGGAGTCAGAATCTACT
sh <i>MEK3</i> (NM_002756.4)	GCTGATGACTTGGTGACCATC
sh <i>MEK6</i> (NM_002758.4)	GATTTAGACTCCAAGGCTTGC

Table 1. Shown are shRNA sequences.

Gene	Forward primer (5' to 3')	Reverse primer (5' to 3')
<i>ROBO1</i>	GACAAAACCCTTCGGATGTCA	CCAGTGGAGAGCCATCTTTCT
<i>SLIT2</i>	GCGAAGCTATACAGGCTTGAT	TGCAGTCGAAAAGTCCTAAGTTT
<i>Robo1</i>	GACAAAACCCTTCGGATGTCA	CCAGTGGAGAGCCATCTTTCT
<i>Slit2</i>	CACGTGCGTCTGTCCTGAAGGCT	TCTCCCAGGTAGCCAGGCAAACAC
<i>Cd133</i>	CCTTGTGGTTCTTACGTTTGTTG	CGTTGACGACATTCTCAAGCTG
<i>Cd44</i>	TCGATTTGAATGTAACCTGCCG	CAGTCCGGGAGATACTGTAGC
<i>Krt19</i>	GGGGTTCAGTACGCATTGG	GAGGACGAGGTCACGAAGC
<i>18S</i>	TGCGAGTACTCAACACCAACA	GCATATCTTCGGCCCACA

Table 2. Shown are primer sequences used in this article.

Figures

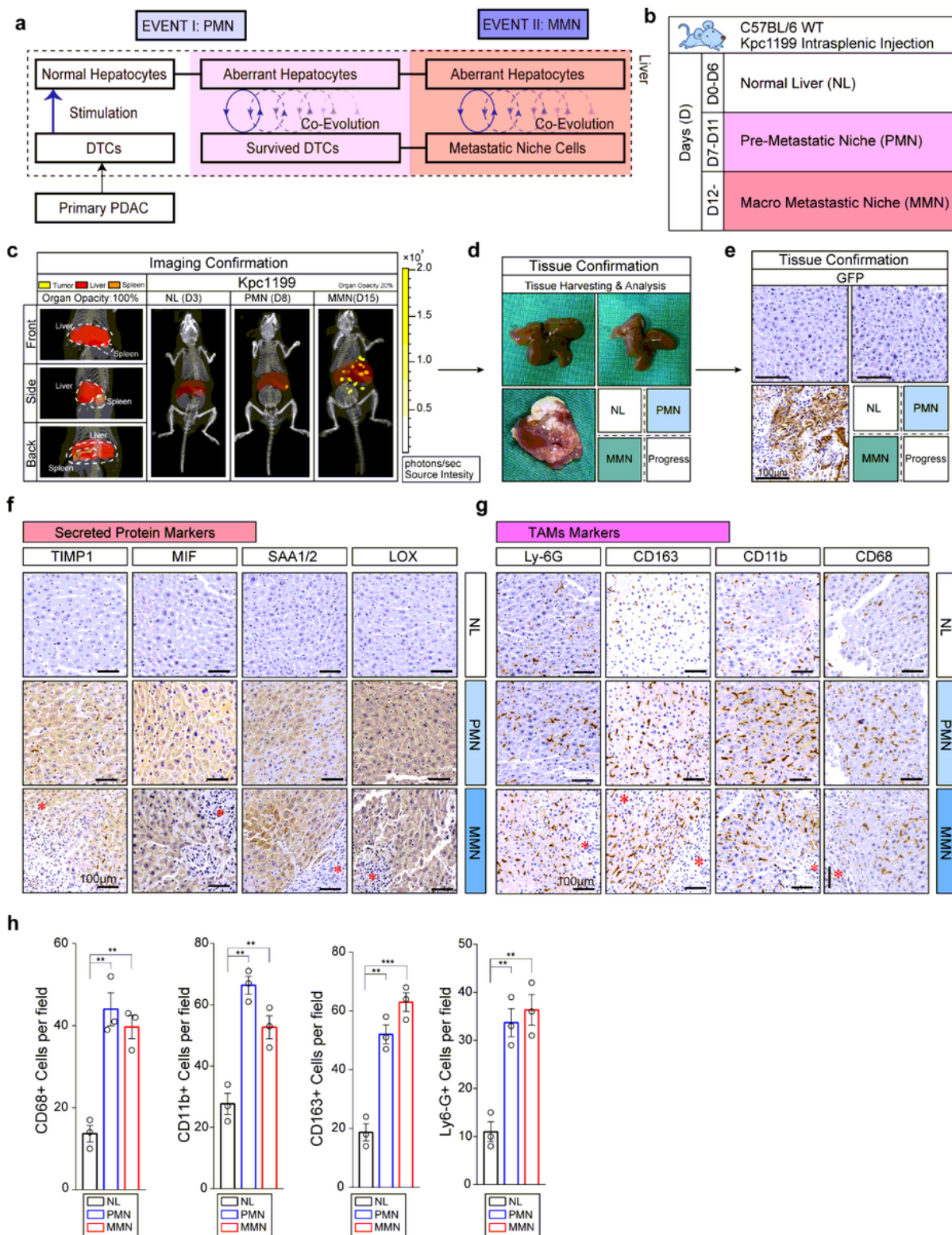


Figure 1

Definition of co-evolution stages

(a) Shown is recognition on progress of co-evolution between DTCs and hepatocytes in liver metastasis of PDAC. (b) Brief procedure displaying intrasplenic injection model for liver metastasis progress study. (c) Liver metastasis model established by intrasplenic injection of murine Kpc1199^{luc}

cells followed by CT combined 3D organ reconstruction bioluminescence imaging assessing the time point of metastasis. Left: front, side, or back view. Right: mice experienced intrasplenic injection photographed on progress NL (day 3 D3), PMN (day 8, D8) and MMN (day 15, MMN). Red, reconstructed liver; orange, reconstructed spleen; yellow, signals of tumor niches. Reconstructed organs opacity, left, 100%; right, 20%. Scale color bar: 2.00×10^5 - 2.00×10^7 . (n=5 mice per group). **(d)** Representative livers of liver metastasis mouse models on progress NL (D3), PMN (D8) or MMN (D15) after injection (n=5 mice per group). **(e)** Shown is the respective IHC-P staining of GFP on left lobules of mouse models on progress NL (D3), PMN (D8) or MMN (D15) (n=5 samples per group, 3 fields assessed per sample). Scale bars, 100 μ m. **(f)** Representative IHC-P staining of PMN specific secreted protein markers: LOX, SAA1/2, MIF or TIMP1 on left lobules of livers of mice model on progress NL (D3), PMN (D8) or MMN (D15) (n=5 samples per group, 3 fields assessed per sample). Scale bars, 100 μ m. * represented metastatic niches. **(g-h)** Representative IHC-P staining of PMN residing TAMs markers: CD68, CD11b, CD163 or Ly-6G in left lobules of livers of mouse models on progress NL (D3), PMN (D8) or MMN (D15) (n=5 samples per group, 3 fields assessed per sample). Scale bars, 100 μ m. * represented metastatic niches. (n=5 samples per group, 3 fields assessed per sample). **, $P < 0.01$; ***, $P < 0.001$.

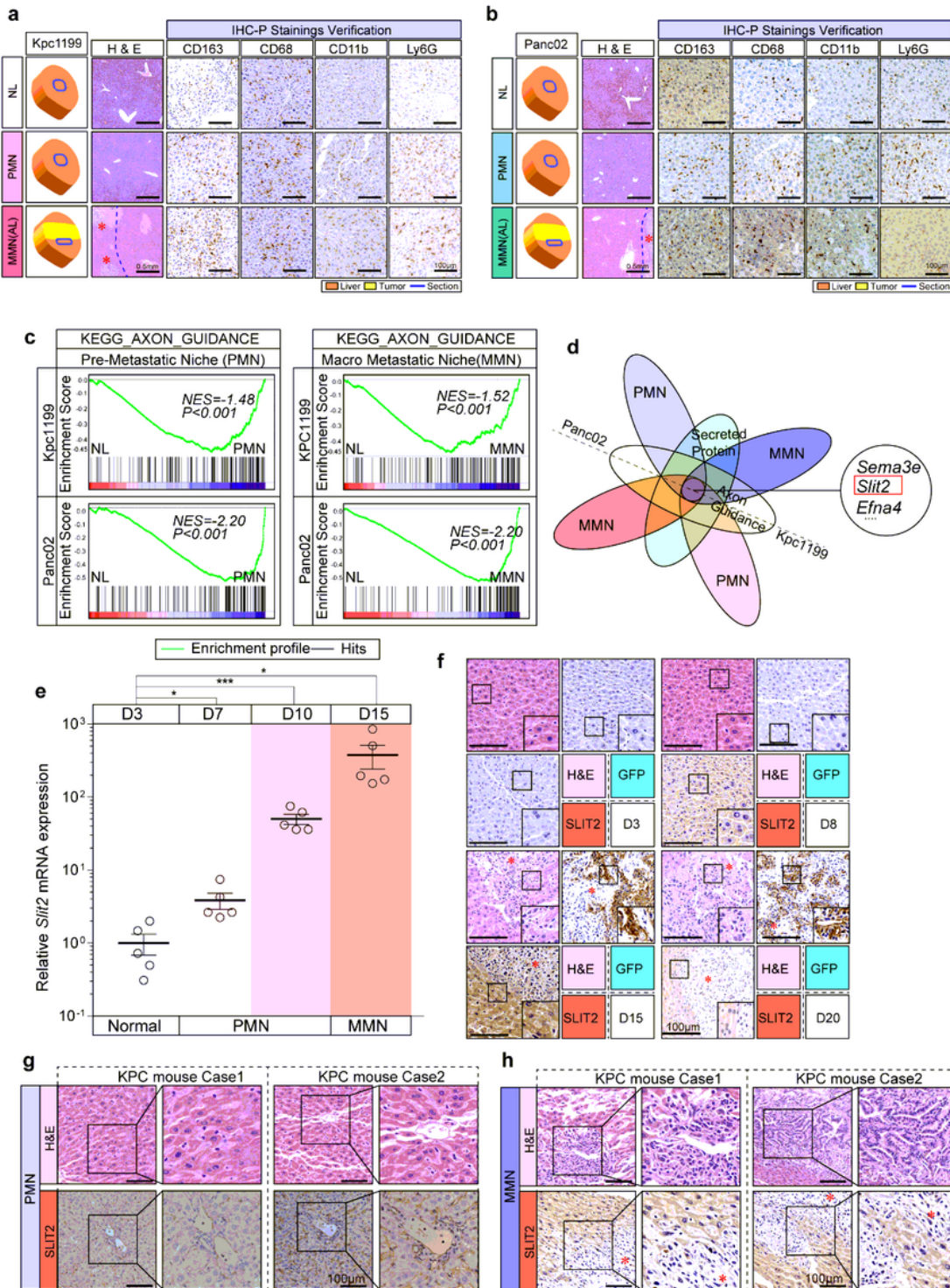


Figure 2

SLIT2 is critical for co-evolution

(a-b) Livers of intrasplenic injection mouse models of Kpc1199 (a) or Panc02 (b) on progress NL, PMN and MMN are performed transcriptional analysis after confirmation of PMN markers (e.g., CD163 etc.) (n=3 mice per group, 5 fields assessed per sample). Scale bars, 500µm for H&E staining or 100µm for

IHC-P. * represented metastatic niches. **(c)** GSEA based on the gene expression profiles of liver tissues on different metastasis progress after mice modeling by Panc02 or Kpc1199 cells. NES, normalized enrichment score. **(d)** Venn diagram displaying secreted axon guidance genes upregulated both in PMN and MMN compared to those in NL for Panc02 and Kpc1199 based on the gene expression profiles of liver tissues of mouse models. **(e)** Real-time PCR showing relative mRNA levels of SLIT2 in left lobule of livers of Kpc1199 injected mouse models on D3, D7, D10 or D15. (n=5 per group, mean±s.e.m.; two tailed unpaired *t*-test). *, *P*<0.05; ***, *P*<0.001. **(f)** Representative IHC-P staining of H&E, GFP or SLIT2 in left lobule of livers of Kpc1199 injected mouse models on D3 (NL), D8 (PMN), D15 or D20 (MMN) (n=5 samples per group, 3 fields assessed per sample). * represented metastatic niches. Scale bars, 100µm. **(g-h)** Representative H&E or IHC-P staining of SLIT2 in PMN **(g)** or MMN **(h)** formed left lobule of livers of KPC mice bearing spontaneous liver metastasis of PDAC (n=6 samples per group, 3 fields assessed per sample). Scale bars, 100µm.

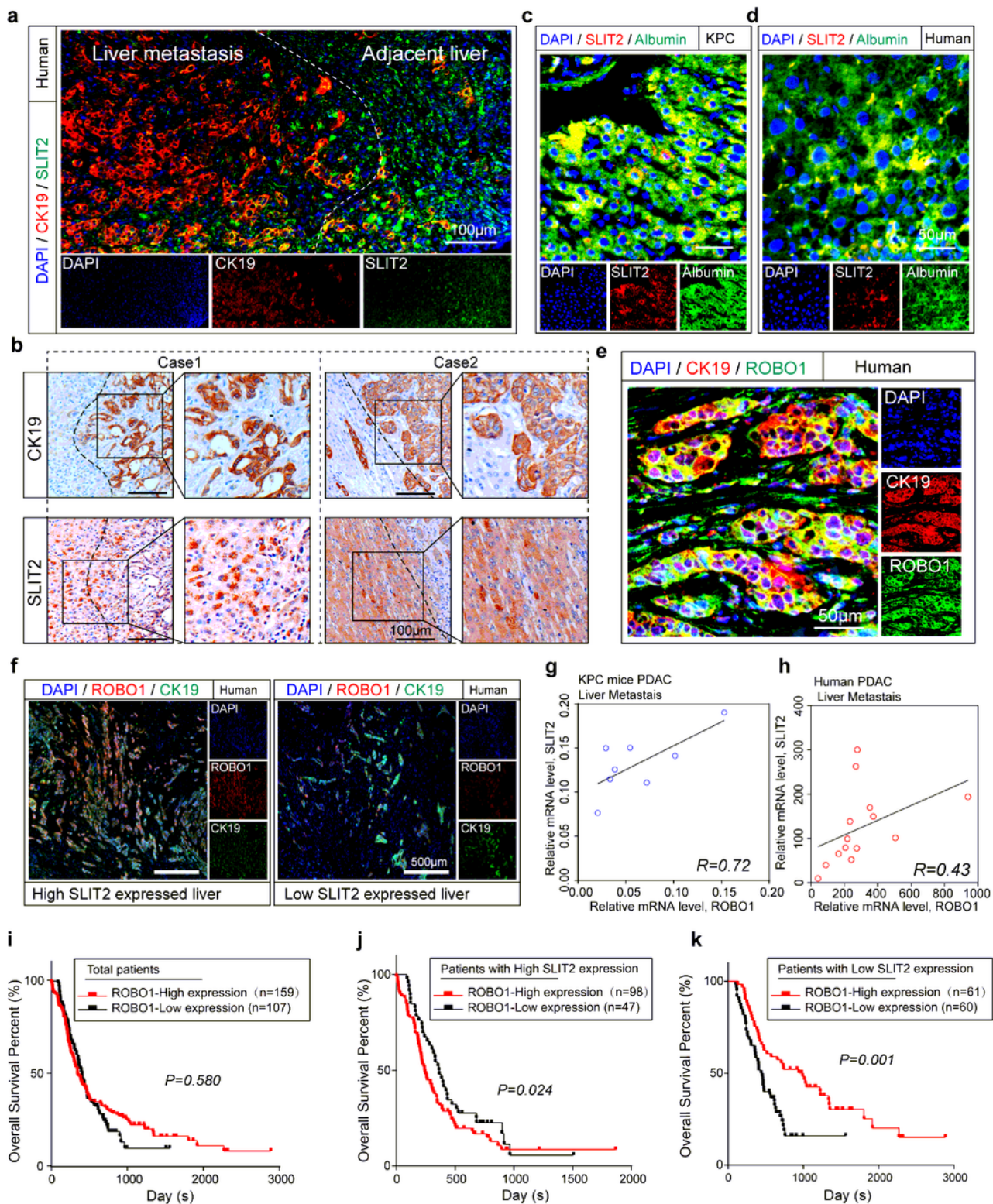


Figure 3

Detecting of SLIT2 and ROBO1 distribution in liver metastasis and related prognosis

(a) Representative IF staining showing the location of SLIT2 and CK19 in adjacent liver or liver metastasis of PDAC patients. SLIT2, green; CK19, red; DAPI, blue (n=35 patients, 3 fields assessed per sample). Scale bar, 100µm. (b) Representative IHC-P staining of CK19 and SLIT2 in liver metastatic

niches of PDAC patients (n=35 cases, 3 fields assessed per sample). Scale bars, 100µm. **(c-d)** Representative IF staining showing the location of SLIT2 and Albumin in PMN of intrasplenic mouse models **(c)** or adjacent liver of metastatic niches of PDAC patients **(d)**. Albumin, green; SLIT2, red; DAPI, blue. (n=35 samples for patients, n=6 samples per group for mouse models, 3 fields assessed per sample). Scale bars, 50µm. **(e)** Representative IF staining showing the location of ROBO1 and CK19 in liver metastasis of PDAC patients. ROBO1, green; CK19, red; DAPI, blue. (n=35 samples, 3 fields assessed per sample). Scale bar, 50µm. **(f)** Shown is representative IF staining displaying expressions of ROBO1 in metastasized livers with or without SLIT2 enrichment. CK19, green; ROBO1, red; DAPI, blue. (n=6 mice per group, 3 fields assessed per sample). Scale bar, 500µm. **(g)** Shown is correlation analysis on ROBO1 and SLIT2 mRNA levels in liver metastasis of KPC spontaneous PDAC liver metastasis model (n=8 mice). **(h-i)** Kaplan-Meier analysis evaluating the relationship of ROBO1 expression and prognosis in PDAC patients with high SLIT2 expression **(h)** or low SLIT2 expression **(i)** according to scores on IHC-P staining on primary tumors (n=266 cases).

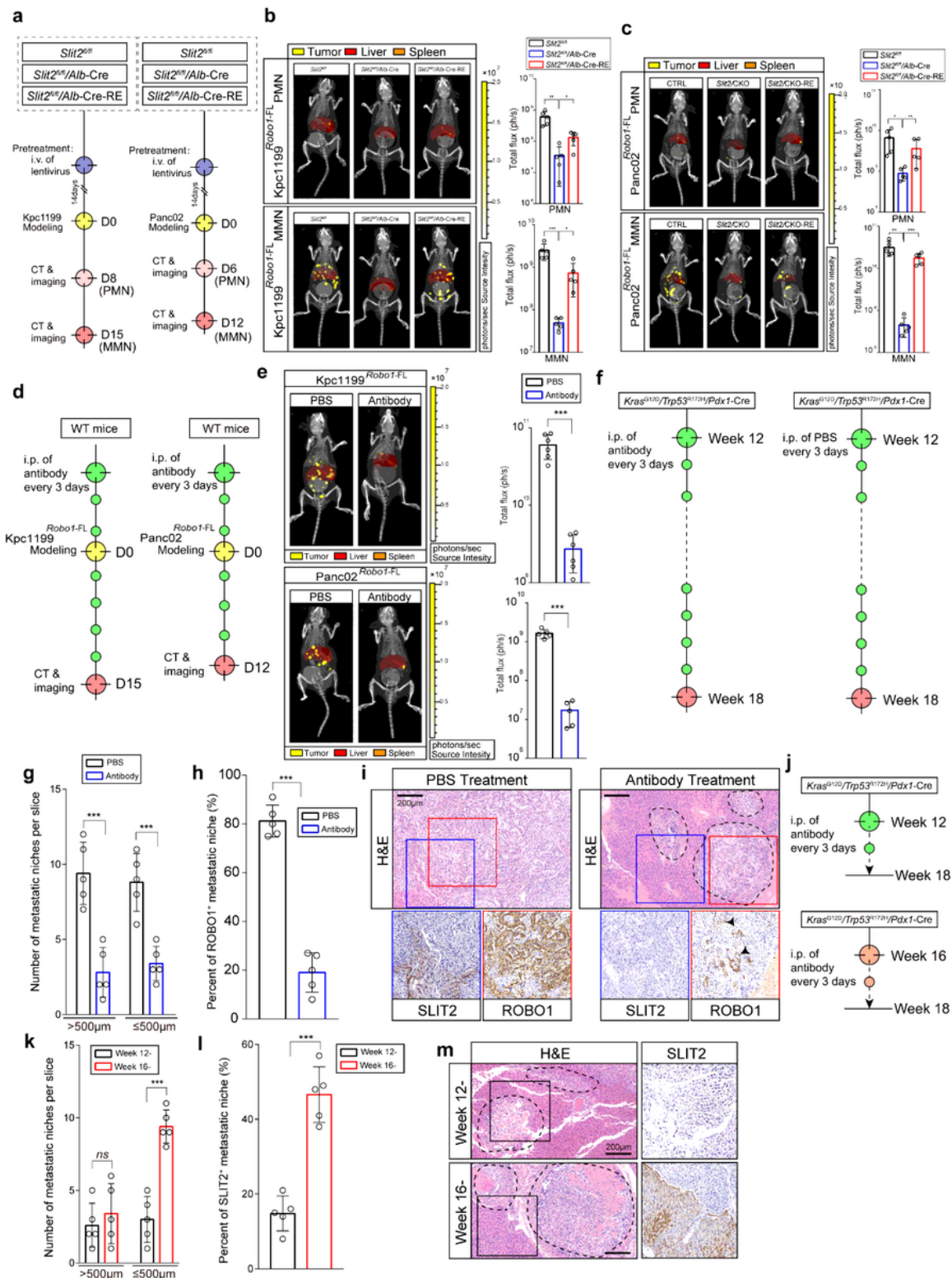


Figure 4

SLIT2-ROBO1 axis facilitates metastasis in liver

(a-c) Representative CT combined 3D organ reconstruction bioluminescence imaging assessing liver metastasis modeled by Kpc1199^{Robo1-FL} (b) or Panc02^{Robo1-FL} (c) on *Slit2*^{fl/fl} or *Slit2*^{fl/fl}/*Alb-Cre* mice with or without Lenti-*loxP-Slit2* injection on progress PMN (upper) and MMN (lower) (n=5 mice per group,

mean±s.e.m.; two tailed unpaired *t*-test). Scale color bars: 2.00×10^5 - 2.00×10^7 . *, $P < 0.05$; **, $P < 0.01$; ***, $P < 0.001$. Red, reconstructed liver; orange, reconstructed spleen; yellow, signals of tumor niches. **(d-e)** Representative CT combined 3D organ reconstruction bioluminescence imaging displaying Kpc1199^{Robo1-FL} (upper) and Panc02^{Robo1-FL} (lower) injected liver metastasis mouse models administrated by PBS or ROBO1 neutralizing antibody (n=5 mice per group, mean±s.e.m.; two tailed unpaired *t*-test). Scale color bar: 2.00×10^5 - 2.00×10^7 . ***, $P < 0.001$. Red, reconstructed liver; orange, reconstructed spleen; yellow, signals of tumor niches. **(f-h)** Shown is administration of PBS or ROBO1 neutralizing antibody on KPC mice for treatment of liver metastasis of spontaneous PDAC from week 12. The number of metastatic niches in liver with diameters over or under 500µm in each group was performed **(g)** and the percent of ROBO1⁺ metastatic niches in each group was also assessed **(h)** (n=5 mice per group, mean±s.e.m.; two tailed unpaired *t*-test; ***, $P < 0.001$). **(i)** IHC-P of SLIT2 and ROBO1 staining on serial sections of KPC liver metastasis with or without ROBO1 neutralizing antibody treatment showing disturbing effect of this treatment on co-evolution in metastasis progress (n=5 mice per group, 3 fields assessed per sample). Scale bar, 200µm. **(j-l)** IHC-P of SLIT2 and ROBO1 staining on serial sections of KPC liver metastasis experienced ROBO1 neutralizing antibody treatment starting from PMN (Week 12-) or MMN (Week 16-) displaying the importance of treatment from initiation of co-evolution. The number of metastatic niches in liver with diameters over or under 500µm in each group was performed **(k)** and the percent of ROBO1⁺ metastatic niches in each group was also assessed **(l)** (n=5 mice per group, mean±s.e.m.; two tailed unpaired *t*-test; ***, $P < 0.001$; ns, no significant difference). **(m)** IHC-P staining of SLIT2 on serial sections of KPC liver metastasis experienced ROBO1 neutralizing antibody treatment starting from PMN (Week 12-) or MMN (Week 16-) indicating the co-evolution interference could be made in early PMN (n=5 mice per group, 3 fields assessed per sample). Scale bar, 200µm.

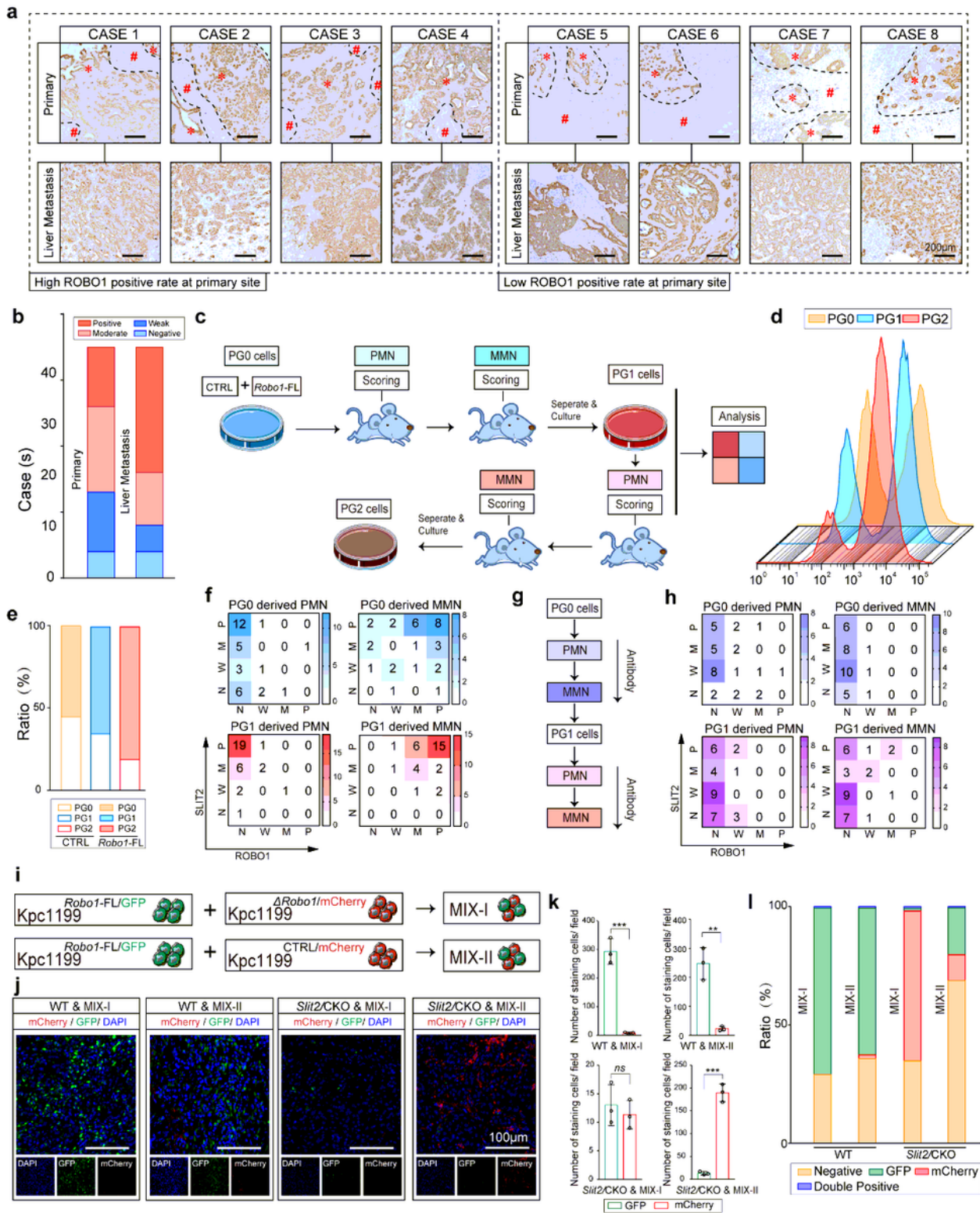


Figure 5

Co-evolution is mediated by SLIT2-ROBO1 axis

(a) Representative IHC-P staining of ROBO1 on human PDAC primary tumors and paired liver metastatic niches displaying the importance of ROBO1 in liver metastasis (n=35 cases, 3 fields assessed per sample). Scale bars, 100µm. * represented ROBO1⁺ metastatic niches; # represented ROBO1⁻ metastatic

niches. **(b)** Shown is number of cases expressing different ROBO1 levels in PDAC primary tumors or liver metastasis according to scores on IHC-P staining (n=35 cases). **(c)** Equal amount of Panc02^{Ctrl} and Panc02^{Robo1-FL/GFP} cells were mixed for intrasplenic injection model followed by metastatic niche separation and re-culture. IHC-P and flow cytometry were performed to evaluate co-evolution. PG0: original cell mixture; PG1: cells derived from PG0 modeled liver metastasis; PG2: cells derived from PG1 modeled liver metastasis. **(d-e)** Shown is flow cytometry detecting cell composition of PG0, PG1 or PG2 (n=5 repeats per group). **(f)** Heat map showing the distribution of ROBO1 and SLIT2 expressions in livers of Panc02 cell mixture modeled mice measured by IHC-P staining (n=32 mice per group, 3 fields assessed per sample; independent experiments for each group). N: negative; W, weak; M, moderate; P, positive. **(g-h)** Mice treated with ROBO1 neutralizing antibody were modeled by Panc02 mixture before IHC-P staining were performed. Heat map displayed the distributions of ROBO1 and SLIT2. (n=32 mice per group, 3 fields assessed per sample; independent experiments for each group). N: negative; W, weak; M, moderate; P, positive. **(i)** Shown is strategy of exploring co-evolution mechanism mediated by SLIT2-ROBO1 in liver metastatic niches. Mixture of equal amount of Kpc1199^{Robo1-FL/GFP} cells and Kpc1199^{ΔRobo1/mCherry} cells (Mix-I) or Kpc1199^{Robo1-FL/GFP} cells and Kpc1199^{CTRL/mCherry} cells (Mix-II) were intrasplenically injected into *Slit2/CKO* or CTRL mice for further examination. **(j-k)** Representative IF staining on Kpc1199 cell mixture formed liver metastatic niches indicating co-evolution (n=5 mice per group, 3 fields assessed per sample, mean±s.e.m.; two tailed unpaired *t*-test). GFP, green; mCherry, red; DAPI, blue. Scale bars, 100μm. *******, *P*<0.001, *ns*.no significant difference. **(l)** Shown is flow cytometry detecting the ratio of two kinds of Kpc1199 cells in separated liver metastatic niches.

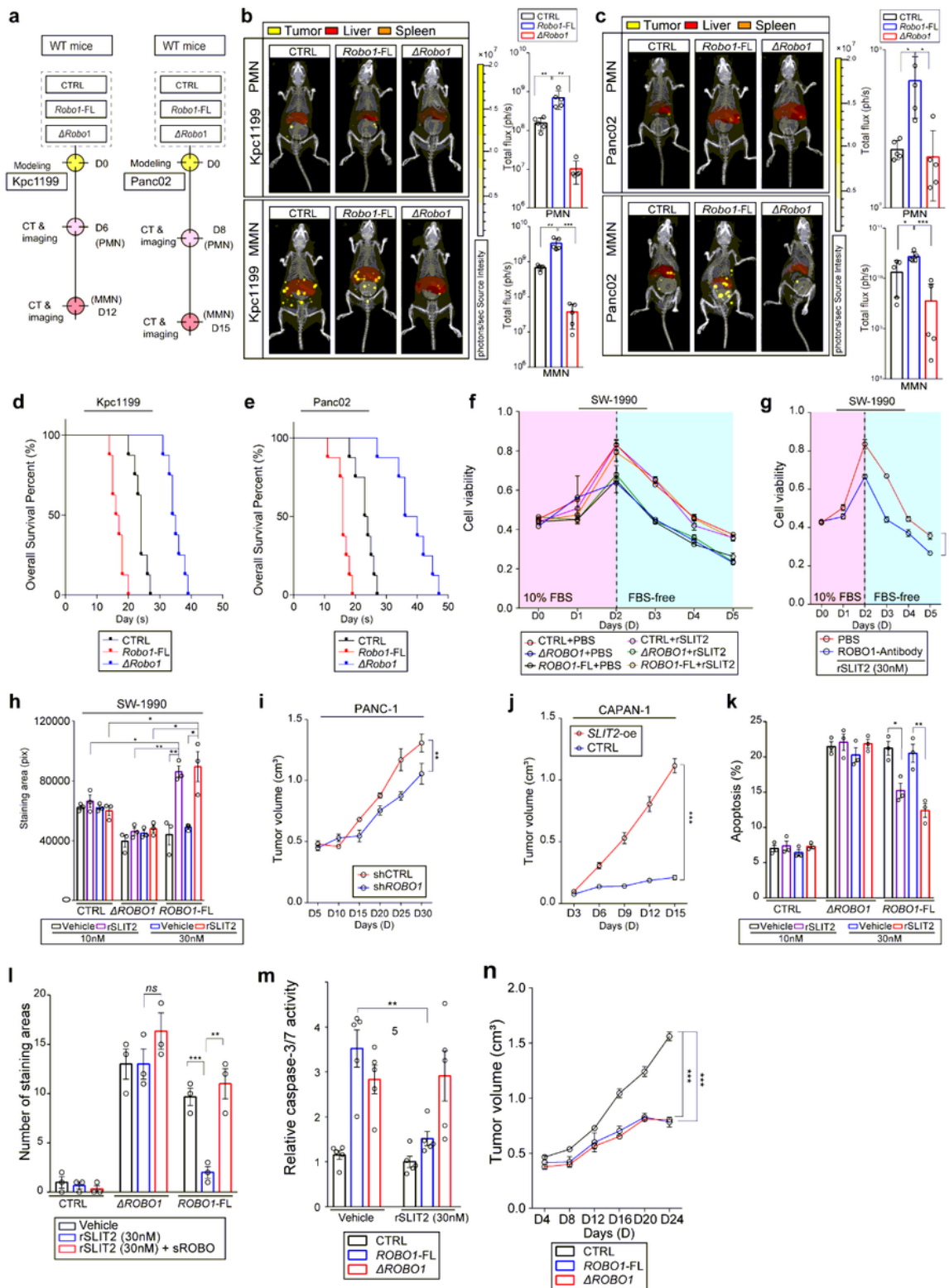


Figure 6

ROBO1 performs characteristics of DR

(a-c) Representative CT combined 3D organ reconstruction bioluminescence imaging displaying the outgrowth ability of Kpc1199^{CTRL}, Kpc1199^{Robo1-FL} and Kpc1199^{ΔRobo1} (b) or Panc02^{CTRL}, Panc02^{Robo1-FL} and Panc02^{ΔRobo1} (c) in mouse models on progress PMN (upper) and MMN (lower) (n=5 mice per group,

mean±s.e.m.; two tailed unpaired *t*-test). Scale color bars: 2.00×10^5 - 2.00×10^7 . *, $P < 0.05$; **, $P < 0.01$; ***, $P < 0.001$. Red, reconstructed liver; orange, reconstructed spleen; yellow, signals of tumor niches. **(d-e)** Survival analysis on intrasplenic mouse models bearing Kpc1199^{CTRL}, Kpc1199^{Robo1-FL} and Kpc1199^{ΔRobo1} **(d)** or Panc02^{CTRL}, Panc02^{Robo1-FL} and Panc02^{ΔRobo1} **(e)** (n=8 mice per group). **(f)** Cell viability of SW-1990^{CTRL}, SW-1990^{ΔROBO1} and SW-1990^{ROBO1-FL} with (+rSLIT2) or without (+PBS) 30nM rSLIT2 exposure, P values are as follows: CTRL+PBS vs ΔROBO1+PBS: $P < 0.001$, CTRL+PBS vs ROBO1-FL+PBS: $P < 0.001$, ΔROBO1+PBS vs ROBO1-FL+PBS: $P = 0.580$, CTRL+rSLIT2 vs ΔROBO1+rSLIT2: $P < 0.001$, CTRL+rSLIT2 vs ROBO1-FL+rSLIT2: $P = 0.850$, ΔROBO1+rSLIT2 vs ROBO1-FL+rSLIT2 $P < 0.001$, ΔROBO1+PBS vs ΔROBO1+rSLIT2: $P = 0.927$, ROBO1-FL+PBS vs ROBO1-FL+rSLIT2: $P < 0.001$ (n=5 repeats per group, mean±s.e.m. Repeat measures ANOVA). **(g)** Cell viability of SW-1990^{ROBO1-FL} exposed with 30nM rSLIT2 with or without ROBO1 neutralizing antibody (n=5 repeats per group, mean±s.e.m. Repeat measures ANOVA). ***, $P < 0.001$. **(h)** Colony formation assay evaluating outgrowth ability of SW-1990 expressed ROBO1-FL or ΔROBO1 exposed to 10nM or 30nM rSLIT2 (n=3 repeats per group, mean±s.e.m.; two tailed unpaired *t*-test); ***, $P < 0.001$. **(i)** Shown is the growth of tumor sizes of subcutaneous xenograft models utilizing PANC-1^{shCTRL} or PANC-1^{shROBO1} (n=7 mice per group, tumor volumes are calculated as volume = $0.5 \times \text{length} \times \text{width}^2$, mean±s.e.m. Repeat measures ANOVA). **, $P < 0.01$. **(j)** Shown is the growth of tumors sizes of subcutaneous xenograft models utilizing CAPAN-1^{CTRL} or CAPAN-1^{SLIT2-oe} (n=6 mice per group, tumor volumes are calculated as volume = $0.5 \times \text{length} \times \text{width}^2$, mean±s.e.m. Repeat measures ANOVA). ***, $P < 0.001$. **(k)** Cell apoptosis of SW-1990^{CTRL}, SW-1990^{ΔROBO1} and SW-1990^{ROBO1-FL} with or without rSLIT2 administration (10nM or 30nM) measured by flow cytometry with dual staining of PI and Annexin V (n=3 tests per group, mean±s.e.m.; two tailed unpaired *t*-test). *, $P < 0.05$; **, $P < 0.01$. **(l)** TUNEL assay performed on SW-1990^{CTRL}, SW-1990^{ΔROBO1} and SW-1990^{ROBO1-FL} with or without 30nM rSLIT2 exposure; for blocking, sROBO administration is performed to SW-1990^{ROBO1-FL} with rSLIT2 exposure (3 fields assessed per sample, mean±s.e.m., two tailed unpaired *t*-test). *ns.no significant difference*, $P > 0.05$, **, $P < 0.01$, ***, $P < 0.001$). TUNEL staining, green; DAPI, blue. Scale bars: 50μm. **(m)** Caspase-3/7 activity in SW-1990^{CTRL}, SW-1990^{ΔROBO1} and SW-1990^{ROBO1-FL} measured at 48 hours after serum starvation in the presence of rSLIT2 at a concentration of 30nM or not (n=5 tests per group, mean±s.e.m., two tailed unpaired *t*-test). **, $P < 0.01$. **(n)** Shown is the growth of tumors sizes of subcutaneous xenograft models utilizing SW-1990^{CTRL}, SW-1990^{ΔROBO1} and SW-1990^{ROBO1-FL} every 4 days (n=6 mice per group, tumor volumes are calculated as volume = $0.5 \times \text{length} \times \text{width}^2$, mean±s.e.m. Repeat measures ANOVA). ***, $P < 0.001$.

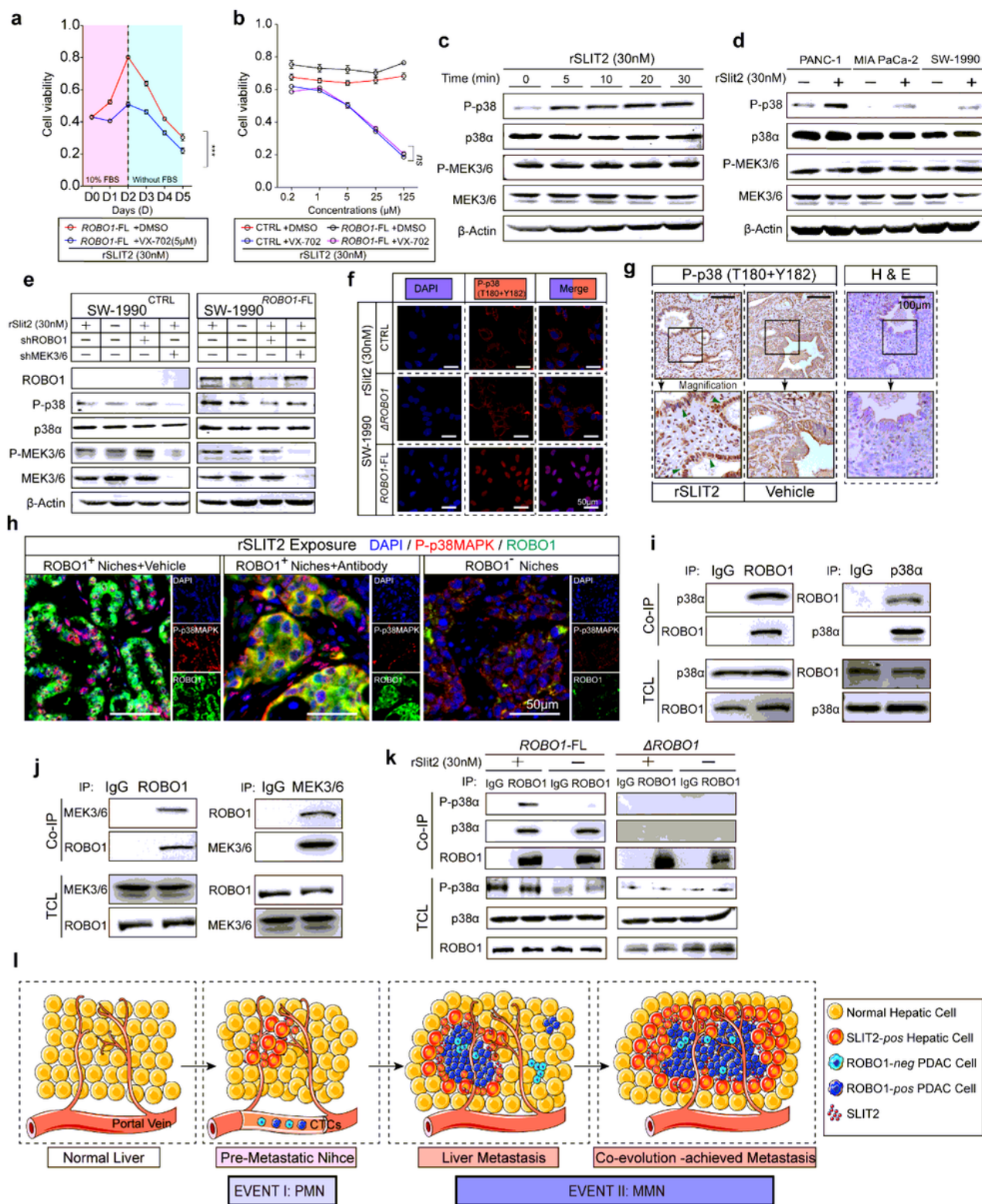


Figure 7

SLIT2-ROBO1 axis triggers p38aMAPK

(a) Cell viability of SW-1990^{ROBO1-FL} exposed with 30nM rSLIT2 with or without p38aMAPK specific inhibitor VX-702 (5μM) (n=5 repeats per group, mean±s.e.m. Repeat measures ANOVA). ***, $P < 0.001$. (b) Cell viability of SW-1990^{CTRL} and SW-1990^{ROBO1-FL} with 30nM rSLIT2 with or without p38aMAPK specific

inhibitor VX-702 at various concentration 0.2 μ M, 1 μ M, 5 μ M, 25 μ M, 125 μ M Time point=D3; n=5 repeats per group, mean \pm s.e.m. Repeat measures ANOVA). *ns.no significant difference, P>0.05.* (c) WB displaying the time dependent manner of rSLIT2 induced p38 α MAPK phosphorylation in SW-1990^{Robo1-FL}. (d) WB showing the phosphorylation of p38 α MAPK in PANC-1, MIA PaCa-2 or SW-1990 cell lines with 30nM rSLIT2 administration. (e) WB displaying the relationship of SLIT2 (30nM), ROBO1 and MEK3/6 expression with phosphorylation of MEK3/6 or p38 α MAPK. (f) Representative ICC staining in 30nM rSLIT2 treated SW-1990^{CTRL}, SW-1990 ^{Δ ROBO1} and SW-1990^{ROBO1-FL} displaying the nuclear translocation of p38 α MAPK (3 fields assessed per sample). P-p38MAPK, red; DAPI, blue. Scale bars: 50 μ m. (g) Representative *ex vivo* IHC-P staining of P-p38 showing rSLIT2 induced phosphorylation of p38 α MAPK in cultured Panc02^{Robo1-FL} metastasized mouse livers (n=6 samples per group, 3 fields assessed per sample). Scale bars, 100 μ m. (h) Representative *ex vivo* IF staining of P-p38 and ROBO1 on KPC mice metastatic niches formed livers with or without ROBO1 neutralizing antibody treatment. ROBO1, green; P-p38MAPK, red; DAPI, blue (n=3 mice per group, 3 fields assessed per sample). Scale bar, 50 μ m. (i-j) Lysate of PANC-1 cell line endogenously immunoprecipitated with anti-ROBO1 and anti- p38 α MAPK (i) or anti-ROBO1 and anti-MEK3/6 (j) Antibody and immunoblotted with the indicated antibodies. (k) Lysate of rSLIT2 (30nM) induced SW-1990^{ROBO1-FL} and SW-1990 ^{Δ ROBO1} immunoprecipitated with anti-ROBO1 and immunoblotted with the indicated antibodies. (l) Brief model displaying the process of SLIT2-ROBO1 mediated co-evolution of hepatic cells and tumor cells which promotes the metastatic niche outgrowth of PDAC.

Supplementary Files

This is a list of supplementary files associated with this preprint. Click to download.

- [Onlinefloatimage8.png](#)
- [Onlinefloatimage9.png](#)
- [Onlinefloatimage10.png](#)
- [Onlinefloatimage11.png](#)
- [Onlinefloatimage12.png](#)
- [Onlinefloatimage13.png](#)
- [Onlinefloatimage14.png](#)
- [Onlinefloatimage15.png](#)
- [Onlinefloatimage16.png](#)
- [Onlinefloatimage17.png](#)
- [Onlinefloatimage18.png](#)
- [Onlinefloatimage19.png](#)
- [Onlinefloatimage20.png](#)